Engineering Science and Technology, an International Journal 35 (2022) 101166

HOSTED BY

Contents lists available at ScienceDirect

Engineering Science and Technology, an International Journal

journal homepage: www.elsevier.com/locate/jestch

Novel fuzzy 1PD-TI controller for AGC of interconnected electric power systems with renewable power generation and energy storage devices

Emre Çelik [a,*], Nihat Öztürk [b]

[a] Department of Electrical and Electronics Engineering, Engineering Faculty, Düzce University, Düzce, Turkey
[b] Department of Electrical and Electronics Engineering, Technology Faculty, Gazi University, Ankara, Turkey

ARTICLE INFO

Article history:
Received 16 September 2021
Revised 5 March 2022
Accepted 16 April 2022
Available online 10 June 2022

Keywords:
Automatic generation control
Reheat thermal power system
Multi-source hydro-thermal power system
Renewable energy penetration
Energy storage device
Governor dead band
Generation rate constraint
Salp swarm algorithm

ABSTRACT

The work prepared designs a novel fuzzy 1 + proportional + derivative-tilt + integral (F1PD-TI) controller and applies it to automatic generation control (AGC) of power systems (PSs) with renewable energy sources (RESs) based on solar thermal, wind and fuel cells. The capability of this unique controller is initially tested on a two-area reheat thermal power system and then on a multi-source two-area hydro-thermal power system. To avert the malfunction owing to improper controller parameters, input scaling factors and other parameters of the F1PD-TI controller are meticulously procured using salp swarm algorithm (SSA) by minimizing the value of integral squared error (ISE) criterion. The worth and contribution of SSA optimized F1PD-TI controller are proclaimed by comparing the results with those offered by several latest controllers. Investigations disclose that the advocated approach beats its serious rivals in terms of shorter settling time, less undershoot/overshoot and smaller ISE value of frequency and tie-line power deviations. As more realistic scenarios, RESs uncertainties in wind speed and solar irradiation are studied and energy storage devices are employed to remedy the problem of surplus/deficient power due to the RESs penetration. Moreover, nonlinearities from governor dead band and generation rate constraint are examined. We realize that significantly better performance and relatively easier design are prominent features of our proposal, which may render it a suitable candidate for practical applications.

1. Introduction

There is a close relationship between stable operation of a power system (PS) and system frequency. The frequency should be kept constant for satisfactory operation of a PS, which is accomplished by matching the total power generation to the load demand + losses at all times. Nonetheless, the load demand on the PS varies momentarily and intricately. This leads to existence of generation-load discrepancies. Such an imbalanced power either enters into or drawn from the rotor of a synchronous generator, inducing changes in generator speed and thus in area frequency and tie-line power between neighboring areas. Without control, it is not possible to sustain the balance between power generation and demanded power. Therefore, a control system is required to preserve frequency and tie-line flows within scheduled edges. As the name hints, automatic generation control (AGC) loop automatically and continually regulates frequency-related active power outputs of the generation units to accommodate load variations. Minimizing the transient aberration in area frequency and tie-line power, and forcing their steady-state errors towards zero as quickly as possible are the major tasks of AGC. When considering the modern PSs as complicated, huge and growing systems interconnecting several control areas of dissimilar types, AGC demands the use of a well-designed control technique to supply the end user with qualified, reliable and uninterruptable electric power.

In a PS driven by fossil fuels, air or oxygen is utilized to burn fossil fuels in order to produce heat and steam, which drive generators to provide electricity. Fossil fuels have been utilized at an ever-increasing rate since the start of the industrial revolution. As per the fresh news, more than 80% of the world energy requirement is still met by fossil fuels and the reserves of the principal remaining fossil fuels on earth are limited. On the other hand, fossil fuel combustion results in the major by-products that are toxic gases added to the earth's atmosphere. Such gases act as greenhouse gases and are harmful to our world, playing a vital role in human-induced global warming. As such, to counter the negative effects of increasing greenhouse gas concentrations and alleviate the dependence on fossil fuels, many countries have turned their visions to renewable energy sources (RESs) like wind, solar, tidal,

* Corresponding author.
E-mail address: emrecelik@duzce.edu.tr (E. Çelik).
Peer review under responsibility of Karabuk University.

https://doi.org/10.1016/j.jestch.2022.101166
2215-0986/

Nomenclature

B	frequency bias, puMW/Hz	T_{ae}	AE time constant, s
R	speed governor regulation parameter, Hz/puMW	T_{fc}	FC time constant, s
K_{ps}	PS gain	T_s, T_T	STG time constants, s
K_{ae}	AE gain	T_{wtg}	WTG time constant, s
K_{fc}	FC gain	T_g	thermal governor time constant, s
K_r	reheater gain	T_t	thermal turbine time constant, s
K_s, K_t	STG gains	T_r	reheater time constant, s
K_{wtg}	WTG gain	T_{rh}	time constant of hydro governor transient droop, s
K_n	participation factor for solar thermal and wind power systems	T_R	hydro governor reset time, s
T_{12}	tie line power coefficient, puMW/rad	T_{gh}	hydro governor main servo time constant, s
T_{ps}	PS time constant, s	T_w	water starting time, s

geothermal and electrochemical. Following a series of recent researches in the literature [1–4], RESs based on wind turbine generator (WTG), solar thermal generator (STG), dish-stirling solar thermal system, aqua-electrolyser-fuel cell (AE-FC), solar photovoltaic (PV) have been shown to ameliorate the system performance saliently. Inspired by the potential of above-cited works, RESs like STGs, WTGs and AE-FC units are integrated with the PSs that we utilize in this work.

AGC area has witnessed ever-increasing attention and curiosity for researchers particularly for around one decade. To this end, several PS models, control techniques and optimization algorithms are appeared in this area. Some of them taking advantages of classical controllers are minority charge carrier inspired algorithm tuned I/PI/ID [5], grey wolf optimization (GWO) [6]/hybrid firefly algorithm-pattern search (hFA-PS) [7]/quasi-oppositional differential search algorithm (QODSA) [8] tuned PI/PID, jaya algorithm-invasive weed optimization (JA-IWO) [9]/optics inspired optimization (OIO) [10]/improved stochastic fractal search (ISFS) algorithm [11]/symbiotic organisms search (SOS) [12] tuned PID, SOS tuned PID/PIDN [13,14], hybrid IWO-PS (hIWO-PS) tuned 2DOF-PID [15], biogeography based optimization (BBO) based 3-degree-of-freedom-PID (3DOF-PID) [1], sine–cosine algorithm (SCA) tuned proportional derivative-proportional integral derivative with double derivative filter (PDPID + DDF) [16] and dragonfly search algorithm (DSA) tuned (1 + PD)-PI [17] controllers. It is known that the performance of these conventional controllers is sensitive to operating condition at which the controller gains are obtained. Thus, they may not be a good choice in a PS network where the operating condition varies randomly. To avert this problem and achieve better solution to AGC issue, several other control schemes based on sliding modes [18], H-infinity [19], artificial neural network approach [20], non-linear disturbance observer [21], model predictive control [22,23] have been introduced. These controllers are shown to receive a remarkable success in handling the problem of AGC, but they are suffering from many shortcomings such as complex architecture, heavy computational expense, and longer implementation time. Considering these aspects undermining the practical potential of controllers, fuzzy logic controller (FLC) as an expert system is suggested by the researchers as described next.

FLCs stimulate the human reasoning and decision-making in the form of linguistic rules. They suit very well the systems especially with important uncertainties, complicated and nonlinear nature. Thus, it is common in the relevant field to combine FLC with diverse controllers [24–32]. Among these approaches are hybrid particle swarm optimization-pattern search (hPSO-PS) [24] and bacterial foraging optimization algorithm (BFOA) [25] tuned fuzzy PI (FPI), BFOA [25]/hybrid PSO-levy flight algorithm (hPSO-LFA) [26]/hybrid harmony search-cuckoo optimization algorithm (hHS-COA) [27]/hybrid improved FA-PS (hIFA-PS) [28]/hybrid differential evolution-PSO (hDE-PSO) [29] tuned FPID, hybrid local unimodal sampling-teaching learning based optimization (hLUS-TLBO) [30]/JA [31] tuned FPID with filter (FPIDN) and improved JA tuned fuzzy PD and cascade PI-PD (FPD/PI-PD) [32] controllers. In order to enhance the system dynamics further, fractional order (FO) controllers are also gaining attention owing to their advantageous aspects for more precise modelling and control betterment possibilities. Thus, they have been extensively employed in AGC studies, which conclude the superiority of FO idea over its integer order counterpart. Recently, a FO FPID (FOFPID) controller tuned using ICA [33] and quasi-oppositional HS algorithm [34] has been reported to offer healthier responses than its integer order version for distinct single/multi-area PSs. Other configurations such as whale optimization algorithm (WOA) tuned PIDN-FOPD [35], DSA tuned FOPI-FOPD [36] and ICA tuned FPIDN-FOIDN (C-I$^{\lambda}$D$^{\mu}$N) [4]/FPIDN-FOPIDN [37] have led to important improvements over the results from similar works. In addition to the above works, a feedback controller and a single-interval type-2 FLC (SIT2-FLC) are proposed in [38] for frequency regulation of multi-microgrids, where the controller gains are optimized by an improved version of HS algorithm. A novel fractional gradient descent (FGD) based on a SIT2-FLC is suggested as the main AGC controller, where the footprint of uncertainty (FOU) coefficient of the SIT2-FLC is specifically tuned to enhance the AGC performance [39]. To effectively solve the AGC problem in a shipboard microgrid in presence of time delays between the controller and the sensor as well as the actuator, a single input interval type-2 fuzzy fractional-order PI (SIT2-FFOPI) controller is presented in [40]. A combination of interval type-2 fractional order fuzzy and PI/PD (IT2FOF/PI-PD) controller supervised online adaptive neuro-fuzzy inference system (ANFIS) is proposed for enhancing the damping characteristics of frequency grid oscillations in a modern marine PS [41]. Optimal settings of the controller parameters are achieved by the modified SCA. An adaptive PI controller is proposed in [42] for AGC in islanded microgrids with electric vehicles, where the general type-2 fuzzy logic sets (GT2FLS) is used to tune PI controller parameters online. For achieving the best tuning performance, modified HS algorithm is utilized. For a four-area interconnected PS, a FLC is designed to optimally tune the parameters of PI controller in an adaptive way [43]. Also, self-adaptive modified bat algorithm is applied to gain optimal performance from the FLC. Though these works introduce important contributions to the relevant literature, most of them give rise to complicated control laws and require the tuning of many parameters that often result in an impractical solution for engineering commissioning. On the other hand, practical convenience of the existing controllers in a real-time implementation is an aspect that is usually overlooked in most researches in the relevant field. Consequently, it is a challenge to design a controller that is not only prolific but also suitable

for easy commissioning. This has motivated us to prepare this work.

In the present paper, a novel fuzzy 1 + proportional + deriva tive-tilt + integral (F1PD-TI) controller is designed and applied to interconnected PS models which consider power generation from RESs in addition to conventional generating units. Based on the broad literature survey presented above, it seems that the proposed controller is the first of its kind and thus it deserves further examination. For proper parameter tuning, salp swarm algorithm (SSA) is adopted to optimize input scaling factors and other parameters of the F1PD-TI controller by selecting integral squared error (ISE) criterion as cost function. The selection of SSA as optimizer is justified in Appendix 1. A rigorous comparison between F1PD-TI controller and other latest controllers is established to meticulously validate the remarkable merits of our proposal. Examination of frequency and tie-line power deviations points out that SSA optimized F1PD-TI controller outweighs its competing peers with respect to shorter settling time, less undershoot/overshoot and smaller ISE value of the system responses. The performance of F1PD-TI controller is also validated in presence of RESs intermittency and volatility, and energy storage devices (ESDs) such as battery energy storage system (BESS) and flywheel energy storage system (FESS) are employed to remedy the problem of intermittent power generation from the RESs. Nonlinearities from governor dead band (GDB) and generation rate constraint (GRC) are also taken into account in the system, as a result of which the proposed controller is observed capable of effectively dealing with the system physical constraints without loss of system stability. We conclude that good performance, simplicity and relatively easier controller commissioning in practice are important advantages of our proposal.

The article is organized as follows: Section 2 provides TF block diagrams of the PS models under consideration. The configuration of F1PD-TI controller, review of SSA concept and SSA based controller optimization are introduced in Section 3. Section 4 is dedicated to extensive simulation results and their assessment relative to the existing results. Finally, conclusions of the work are drawn in Section 5.

2. Description of power systems

The examined PSs are interconnected two-area reheat thermal (TART) PS and multi-source two-area hydro-thermal (MSTAHT) PS whose transfer function (TF) models are displayed in Fig. 1(a) [4,13,25,29] and 1(b) [4,6,7,25,30], respectively. Generation areas of both systems are of equal sizes. Each area of TART PS is driven by a single reheat type of thermal turbine whereas there are one non-reheat thermal turbine and one hydro turbine contributing to the total power generation in each area of MSTAHT PS. In addition to the conventional thermal- and hydro-based generation units, renewable energy sources (RESs) are also considered to supply electricity in area-1 of both systems. Moreover, to cancel out the negative effects of surplus/deficient power from the RESs, ESDs such as BESS and FESS are included in each area of MSTAHT PS.

The TF model of the RESs is depicted in Fig. 1(c). As seen, the RESs are composed of two solar thermal generators (STGs), three wind turbine generators (WTGs), one aqua-electrolyser (AE) and two fuel cells (FCs). Solar thermal PS includes solar and thermal parts because sunlight in this generation system is collected and concentrated by parabolic collectors to heat a heat-transfer fluid circulating in the receiver that generates electricity after transforming into steam and mechanical energy in a turbine. In wind PS, wind energy is turned into electrical energy by capturing the wind kinetic energy by the rotor blades of wind turbines. The AE

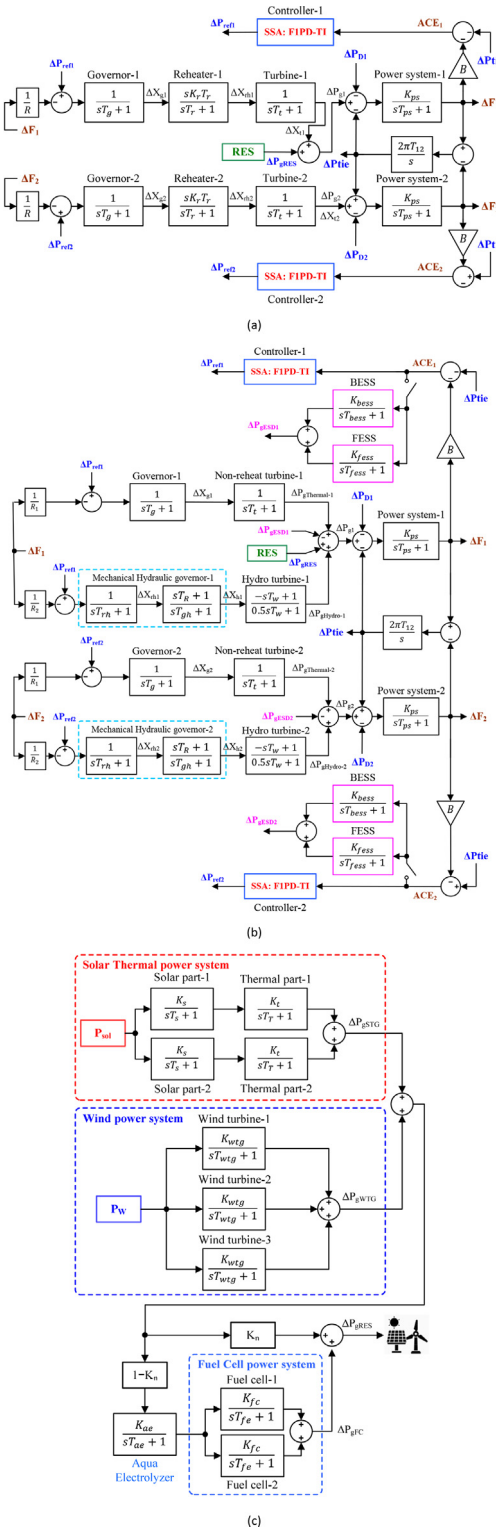

Fig. 1. TF models of (a) TART PS (b) MSTAHT PS and (c) RESs.

produces hydrogen energy to be converted into electricity by the FCs in order to accommodate inconstant power from STGs and WTGs. Here, energy delivered to the AE from STGs and WTGs are adjusted by $1 - K_n$, where K_n is the participation factor in the range [0, 1]. In another words, the contribution of generation in solar thermal and wind power systems to the total RESs generation ΔP_{gRES} is specified by K_n.

Each generation unit of TART PS and MSTAHT PS has its own governing system, turbine and generator. For an area, three inputs and two outputs are existing. The controller output ΔP_{ref} (also known as reference power setting or plant input signal), change in load demand ΔP_D and change in tie-line power ΔP_{tie} are the inputs where the outputs are change in generator frequency ΔF and area control error (ACE). Notice that one extra input ΔP_{gRES} comes from the outcome of RESs integration in area 1 of both systems. Besides, backup system components such as BESS and FESS are connected to the load side of MSTAHT PS to investigate their role against load variations in this system. Using the ACE signal, ESDs adjust their output ΔP_{gESD}, which is fed to the summing point similar to ΔP_{gRES}.

A schematic diagram of the current research is illustrated in Fig. 2. This system can be regarded as a modern PS since it is composed of a class of loads, storage units and renewable generations. DC/AC converters assist in synchronizing STG, FC and energy storing units with the AC bus. Also, AC/AC converter is added to the output of WTG for the synchronization purpose. Transformers are also used to increase and match the output voltages of generation units for the proper interconnection. ESDs can charge/absorb or discharge/release energy from or to the grid within a short period of time if there is a surplus or deficient amount of power, respectively, in the system.

The description of various symbols along with the simulation data are provided in Nomenclature and Appendix 2 at the end of the paper. Further, for a fair comparison, the researcher followed the same test models and original parameters settings as in a recent work given by [4], where a new controller is proposed and shown to be superior to several published methods.

3. Controller synthesis

This section elaborates the proposed F1PD-TI controller structure first, then gives the searching model of SSA approach and finally describes how the SSA is suited to search for the optimal parameters of F1PD-TI controller.

3.1. Controller design

The objective of a controller designed for AGC issue is to match the power generation with demanded power as speedily as possible in order to drive frequency and tie-line power deviations towards zero. Following a step load disturbance (SLD), immediate deviation in frequency and tie-line power flow occurs, which also yields to produce ACE. By acting on the ACE signal, the controller adjusts the load reference setpoint to accommodate variations in system load and accordingly restore system frequency to the nominal value. As the load in PSs is unpredictable, intricate and is changing continually and abruptly, it is necessary to design high-performance controllers to better take over the problematic AGC issue.

The classical PI and its modified cousins are famous for their simple design, inexpensive computational burden and relatively robust performance, which lead to popular use of them in various PSs [5–17]. Yet, their insufficient capacity to deal with nonlinearities and uncertainties make them comparably ineffective to offer a desired level of controlling performance in a large-scale system. In order to avert the shortcomings of classical controllers and boost their performance, FLC is incorporated in the controller design [24–32] to satisfy the challenging control objectives in PS. On the other hand, the performance of several kinds of FO controllers [33–37] have been recognized in the relevant field recently. The performance achieved by these controllers are found to be incremental, but they give birth to complex controller designs owing to several parameters to be tuned accurately. Moreover, the responses reported by them seem that they could be further improved in terms of time-domain specifications. As such, in this paper, F1PD-TI controller is designed and applied as an effective controller to AGC of TART PS and MSTAHT PS. To our best knowledge, there is no previous research proposing F1PD-TI controller in any control engineering area. The configuration of this controller for area 1 is depicted in Fig. 3. Here, the input $\Delta Ptie$ changes sign for different areas, i.e. its sign is negative in area 1 and positive in area 2. As seen in Fig. 3, there are two controllers as F1PD controller and TI controller. In TI controller, a tilted component with a

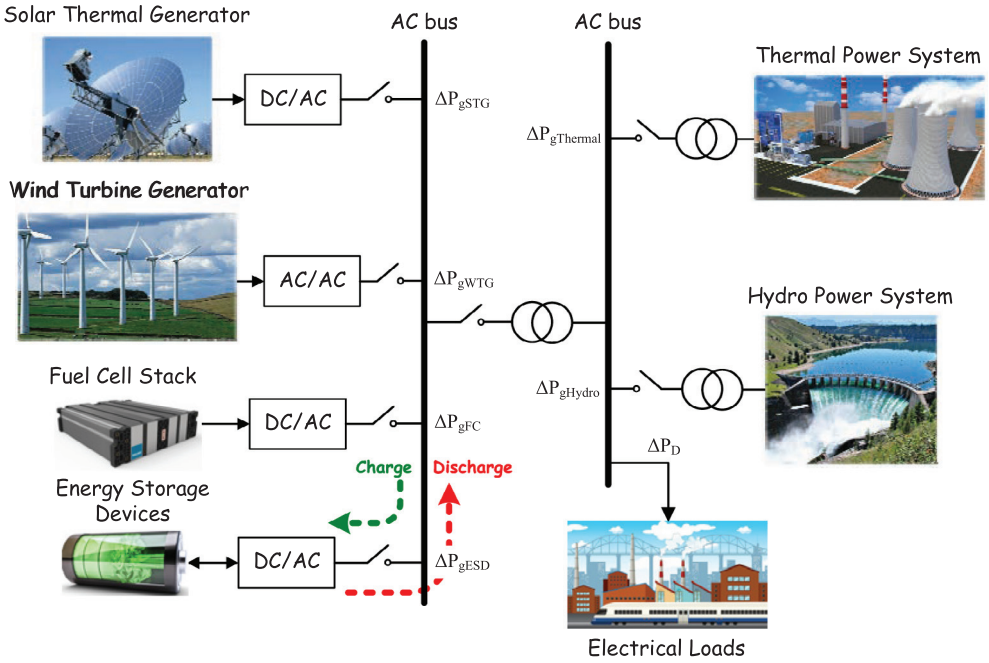

Fig. 2. The schematic diagram of the current research.

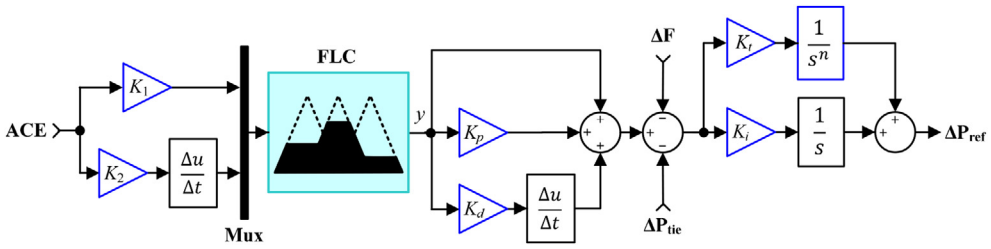

Fig. 3. Configuration of F1PD-TI controller.

transfer function of $s^{-\frac{1}{n}}$, $n \in \mathbb{R}, n > 0$ works as a tilt-type compensator and replaces the proportional component of PI controller. It is also noticeable that the output of F1PD controller is not connected with the input of TI controller directly. Instead, both ΔF and ΔP_{tie} signals are subtracted from the output signal of F1PD controller to form the input signal for the TI controller. The effectiveness of this connection has been discussed in [17], which substantiated its remarkable merits and potential for achieving a better system performance.

The F1PD-TI controller considers ACE and time derivative of ACE as input signals after being scaled by K_1 and K_2, and produces the required plant input signal ΔP_{ref}. As shown in Fig. 1, area-1 and area-2 ACE signals are defined by Eq. (1).

$$\begin{aligned} ACE_1 &= -B\Delta F_1 - \Delta Ptie \\ ACE_2 &= -B\Delta F_2 + \Delta Ptie \end{aligned} \tag{1}$$

where B is the frequency bias, ΔF_i is area frequency error/deviation and ΔP_{tie} is tie-line power error/deviation. Assuming y is the output of FLC, the complete control algorithm equation relating ACE to ΔP_{ref} can be expressed as step down.

$$\Delta P_{ref} = \left(\{y + yK_p + ysK_d\} - \Delta F - \Delta P_{tie}\right) \times \left(\frac{K_t}{s^n} + \frac{K_i}{s}\right) \tag{2}$$

where K_p, K_i, K_d, K_t are proportional, integral, derivative, tilt gains and n is a real number. The fractional power of s in the tilt component is approximated by the CRONE approximation approach by setting the fitting frequency range to $\omega_L = 0.01$ rad/s and $\omega_H = 100$ rad/s, where the approximation order is chosen as $N = 5$. The interested readers can refer to [36,44] for more theoretical descriptions about the CRONE approximation concept. In comparison with the recent controllers, i.e. [4,25,33,37], the proposed F1PD-TI controller is relatively simpler to design with seven tunable parameters (K_p, K_i, K_d, K_t, K_1, K_2, n) and it has one fractional order parameter in the tilt part only, which yield an easy commissioning. Input scaling factors (K_1, K_2), as well as other controller parameters (K_p, K_i, K_d, K_t, n) are to be optimized to evade from poor performance due to improper parameter tuning.

In FLC, seven number of membership functions (MFs) is selected for each input and output variable. In principle, there is no prior knowledge of which of the MF shapes suits best the problem at hand. But, following our comprehensive literature review, triangular MF is found to be more popular than other types, i.e. trapezoidal, bell-shaped, and so forth, due to its fast and simple computation using linear relations. Besides, previous studies on employing FLC [4,37,45] suggests the preference for triangular MF over other alternatives. To justify this preference, an exercise revealing the supreme performance of triangular shape over the others is established in Section 4. Thereof, in the paper, triangular MFs lying over within the range [−1, 1] are adopted for the inputs and output of FLC as shown in Fig. 4, where the linguistic variables are NB (Negative Big), NM (Negative Medium), NS (Negative Small), Z (Zero), PS (Positive Small), PM (Positive Medium) and PB (Positive Big), respectively.

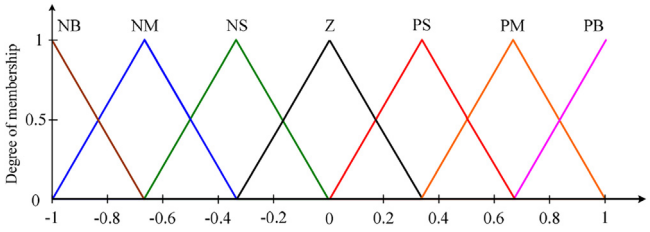

Fig. 4. Triangular MFs for two inputs and one output.

As we have defined seven MFs for each FLC input, $7 \times 7 = 49$ rules are required to be set carefully as provided in Table 1. Here, conditional if-then statements are declared, which try to establish a link correlating ACE and time derivative of ACE with the FLC output variable y like an expert. The function of Table 1 can be expressed by the following rules:

- If ACE is NB and ACE derivative is NB, this implies that the controller output signal ΔP_{ref} is so big at present that u may be NB.
- If ACE is PB and ACE derivative is PB, this implies that the controller output signal ΔP_{ref} is so small at present that u may be PB.
- If ACE is Zero and ACE derivative is Zero, this implies that the controller output signal ΔP_{ref} is in its required value at present, thus u may be Zero.
- If ACE and ACE derivative fulfil the other cases, this implies that the controller output signal ΔP_{ref} is neither too large nor too small; thus u may be a transition value between NB and PB.

For resembling the way of decision making in human beings, Mamdani's min–max fuzzy inference system is deployed and during defuzzification the crisp output y is obtained from the output of FLC using the center of gravity (centroid) technique.

3.2. Review of salp swarm algorithm

Salp swarm algorithm (SSA) is a nature-inspired optimization technique recently proposed in [46]. The aim of SSA is to solve optimization problems by resembling the swarming behavior of salps found in oceans. Satisfactory exploration and exploitation propensities of this algorithm make it captivating for several applications in need of optimization. Indeed, compared to other intricate algorithms, SSA is simple to code and requires low computational power. Besides, there is only one tunable parameter in the algorithm where its value is decreased gradually over the course of iteration to provide exploration for unvisited areas in the early stages of optimization and then exploitation around a promising area in the last stages of optimization.

Similarly to other algorithms, SSA iteratively evolves the individuals (i.e. salps) in the population through its unique search model after initiating them randomly in the feasible region. During

Table 1
Rule table harnessed in the controller.

y		ACE derivative						
		NB	NM	NS	ZE	PS	PM	PB
ACE	NB	NB	NB	NB	NM	NM	NS	ZE
	NM	NB	NM	NM	NM	NS	ZE	PS
	NS	NB	NM	NS	NS	ZE	PS	PM
	ZE	NM	NM	NS	ZE	PS	PM	PM
	PS	NM	NS	ZE	PS	PS	PM	PB
	PM	NS	ZE	PS	PM	PM	PM	PB
	PB	ZE	PS	PM	PM	PB	PB	PB

optimization, the population is classified into two groups as leader and followers. The leader salp stands at the top of the chain, attacking towards the food source F. Each of the remaining salps is assumed to be a follower that follows the salp in front of it. The aligning of salps in this way results in a chain visualized in Fig. 5. Fig. 6..

For m salps in a d-dimensional search space, the positions of all salps are stored in a two-dimensional matrix called X as described in Eq. (4).

$$X = \begin{bmatrix} x_1^1 & x_1^2 & \cdots x_1^{d-1} & x_1^d \\ x_2^1 & x_2^2 & \cdots x_2^{d-1} & x_2^d \\ \vdots & \vdots & \vdots & \vdots \\ x_m^1 & x_m^2 & \cdots x_m^{d-1} & x_m^d \end{bmatrix} \tag{4}$$

Eq. (5) is proposed in SSA to update the position of the leader.

$$x_1^j = \begin{cases} F^j + c_1\left(lb^j + c_2\left(ub^j - lb^j\right)\right), & c_3 \geq 0.5 \\ F^j - c_1\left(lb^j + c_2\left(ub^j - lb^j\right)\right), & c_3 < 0.5 \end{cases} \tag{5}$$

where x_1^j and F^j show the position of the leader and food source in the jth dimension, respectively. c_2 and c_3 are random numbers in the range 0 and 1. Note that F is the best point in the search space achieved so far by the SSA and it is the chain's target. c_1 is the most substantial parameter in the algorithm expressed in Eq. (6) [47].

$$c_1 = 2e^{-(4t/T)^2} \tag{6}$$

where t and T are the iteration index and maximum iteration number, respectively. As t increases, the value of c_1 is reduced which is beneficial for balancing exploration and exploitation. The decreasing trend of c_1 obligates the salps to search with large steps in the initial iterations, while they are forced to search on a small scale in the last iterations. The characteristic of Eq. (6) plays a crucial role in finding the global optimum without stagnating in local optima or facing immature convergence. As for the followers, they change their position simply by.

$$x_i^j = \frac{1}{2}\left(x_i^j + x_{i-1}^j\right) \tag{7}$$

where $i \geq 2$ and x_i^j is the position of the i th salp in the j dimension. The pseudocode description of SSA is given in Algorithm 1.

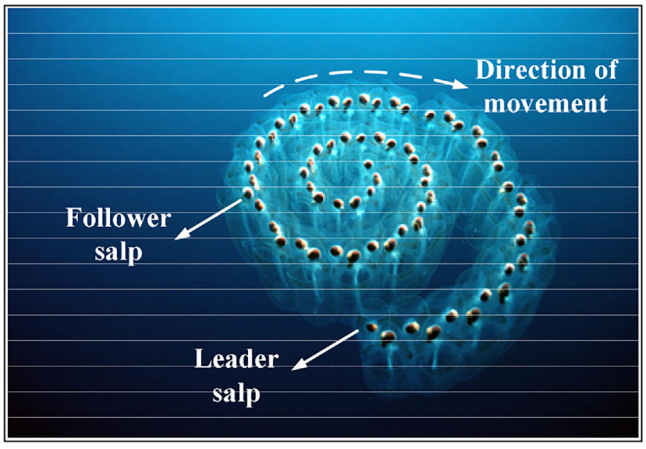

Fig. 5. Visualization of the salps' chain.

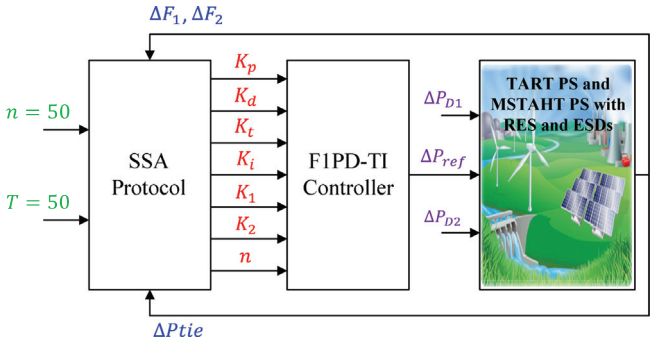

Fig. 6. Block diagram of the optimization process.

Algorithm 1
Pseudocode description of SSA.

```
Initiate the salp population X randomly
while (termination criteria are not satisfied) do
Assess the fitness of each individual (salp)
Set F as the best individual
Update c1 using Eq. (6)
for every salp do
  if (i==1) then
    Amend the position of the leading salp using Eq. (5)
  else
    Amend the position of the follower salp using Eq. (7)
  end
end
Check and ameliorate the salps based on the bounds of
  variables
end
return F
```

The unique merits of SSA such as flexibility, simplicity and good search performance have directed many researchers to take benefits of this algorithm in several applications like classification [48], best conductor selection in a practical radial distribution system [49], optimization of a power system stabilizer [50]/size of a CMOS dif-

ferential amplifier alongside the comparison circuit [51], optimal parameter extraction of fuel cells [52], sizing of PV systems [53], and economic load dispatch [54]. All these researches conclude that SSA is capable of providing good solution quality with a satisfactory convergence trend. This can be attributed to the fact that the method manages a fine balance between exploration and exploitation phases that are switched from one to another progressively. The gradual transition between the two tendencies is accomplished by the parameter c_1 that is adaptive to iteration count.

3.3. Design of F1PD-TI controller using SSA

In the design of a controller where the problem is formulated as an optimization problem, the cost function must be declared first to tune the controller parameters and obtain an optimal controlled response that meets the given control objectives and constraints. The four commonly used cost functions in controller designs are integral of absolute error (IAE), integral of squared error (ISE), integral of time multiplied squared error (ITSE) and integral of time multiplied absolute error (ITAE). For calculating these functions, a particular experiment is performed on the system and the integrals are evaluated over a certain time, generally till a time long enough for the responses to settle. IAE tends to cause a slow response and ITSE provides fast response, but with considerable sustained oscillations because it tolerates large errors at the start of the response owing to weighting errors less heavily. Besides, both ITSE and ITAE based control systems provide large controller output when there is a step change in set point. ITAE also leads to sluggish initial response, but this renders it to reduce the settling time significantly. ISE can be considered as a criterion that eliminates the downside of ITSE criterion since it does not add weight to any of the errors in the response. There are a great number of successful AGC studies that utilize ISE as cost function [4,25,33,37]. That's why ISE is employed in this work to optimize the parameters of F1PD-TI controller. Mathematical expression of the ISE cost function is given in Eq. (8).

$$J = ISE = \int_0^{t_{sim}} \left(\Delta F_1^2 + \Delta F_2^2 + \Delta P_{tie}^2\right) dt \tag{8}$$

where J is the cost function and t_{sim} is the time scale of simulation. In the optimization problem, there are inequality constraints introduced by the parameter bounds of F1PD-TI controller. Consequently, from the viewpoint of optimization, the design problem can be formulated as follows:

Minimize J, subject to:

$K_p^{min} \le K_p \le K_p^{max}, K_i^{min} \le K_i \le K_i^{max}, K_d^{min} \le K_d \le K_d^{max}, K_t^{min} \le K_t \le K_t^{max}, K_1^{min} \le K_1 \le K_1^{max}, K_2^{min} \le K_2 \le K_2^{max}, n^{min} \le n \le n^{max}$ where the superscripts *min* and *max* denote the minimum and maximum values of the respective parameter. Searching for the controller parameters that give the minimum value of J without violating the above constraints is the goal of SSA based optimization process.

The models of the test systems depicted in Fig. 1 are constructed in Matlab/Simulink environment and SSA program is written in M-file script. In SSA, a population size of $n = 50$ and maximum iteration number $T = 50$ have been used. The Simulink models are simulated by considering a SLD of $\Delta P_{D1} = 0.01$ puMW and $\Delta P_{D1} = 0.015$ puMW applied to area-1 of TART PS and MSTAHT PS at $t = 0$ s, respectively. At the same instant, the solar irradiation P_{sol} for all STGs and wind speed P_W for all WTGs are assumed to be 0.001 pu and 0.002 pu, respectively. ΔF_1, ΔF_2 and ΔP_{tie} signals obtained in the Simulink environment for each candidate solution are transferred to the workspace to calculate the cost function J in the optimization algorithm. As per the value of J assigned to every solution, the population of salps is modified and evolved through generations using the main SSA steps given in Eqs. (5)–(7). The best salp found following the termination of SSA has been used in simulation for evaluating the performance of F1PD-TI controller. The following block diagram describes the above process more clearly.

Simulations are performed by Matlab 2017b running on a Windows computer with i5-7400 CPU and 8 GB RAM. The sample time is fixed and set to $h = 0.001$ s. The optimization process was recurred 30 times, and over 50 runs, the optimum parameters of F1PD-TI controller resulting in the minimum value of J are considered as the final controller parameters, which are reported in Table 2 for both TART PS and MSTAHT PS models.

4. Assessment of simulated results

This section evaluates the effectiveness of SSA optimized F1PD-TI controller on two-area reheat thermal PS and multi-source two-area hydro-thermal PS with renewable power generation and energy storage devices. The TF models of these systems are displayed in Fig. 1. A rigorous comparison study with various published control schemes is also presented to show the contribution of our proposal. For each test system, the optimum controller parameters found by applying SSA protocol are reported in Table 2. By inserting these parameters in the controller, system dynamic responses are acquired and provided. The interested readers are kindly referred to Appendix 3 for the calculated system matrices for both TART PS and MSTAHT PS. Settling time (T_s), undershoot (U_s), overshoot (O_s), as well as ISE value of the ΔF_1, ΔF_2 and ΔP_{tie} responses are chosen as time-domain performance criteria among the works to inspect and compare several results quantitatively. In line with [4], a tolerance band of ±0.05% is used to obtain T_s. For convenience, comparably the best results are **bolded** in the respective tables.

4.1. TART PS

The TART PS is simulated under a SLD of $\Delta P_{D1} = 0.01$ puMW in area-1 at $t = 0$ s by using the corresponding controller parameters in Table 2. The obtained dynamic responses of deviation in area-1 frequency (ΔF_1), deviation in area-2 frequency (ΔF_2) and deviation in tie-line power (ΔP_{tie}) are delineated in Fig. 7. To remark the dominance of SSA optimized F1PD-TI controller, its outcomes are contrasted with some recently reported results based on bacterial swarm optimization (BSO) tuned FOPID [55], SOS tuned PIDN [13], hDE-PSO tuned FPID [29], SCA tuned C-PDN-PIDN [16], JA tuned FPIDN [31] and ICA tuned C-I$^{\lambda}$D$^{\mu}$N [4]. It is apparent in Fig. 7 that the F1PD-TI controller performs significantly better than the previous control schemes with regard to enhanced and swift oscillations-free responses that settle to the desired zero steady-state value with negligible overshoot and trivial undershoot.

The associated controller signals in area-1 (ΔP_{ref1}) and area-2 (ΔP_{ref2}) are displayed in Fig. 8. Following the application of SLD to area-1 at $t = 0$ s, ΔP_{ref1} takes a high value initially to reject the given disturbance quickly and then settles to its reference value around 0.05 s. At steady-state, since $\Delta P_{D1} = 0.01$ puMW, this needs

Table 2
Optimized F1PD-TI controller parameters for the systems studied.

Controller parameters	TART PS	MSTAHT PS
K_p	4.9999	2.5955
K_d	0.0511	0.1400
K_t	5.0000	2.4641
K_i	4.5726	2.6559
K_1	7.0037	3.2882
K_2	7.8105	2.0601
n	0.0100	0.0756

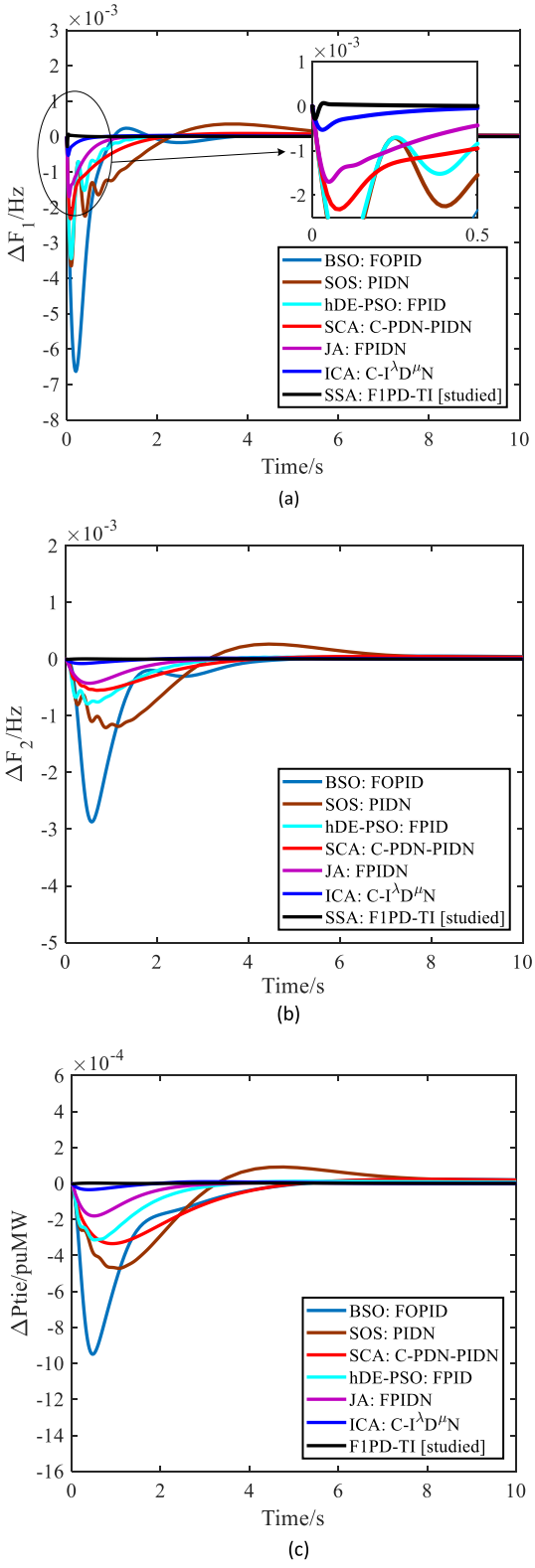

Fig. 7. Comparison of the TART PS responses under $\Delta P_{D1} = 0.01$ puMW (a) ΔF_1 (b) ΔF_2 (c).ΔP_{tie}

ΔP_{ref1} equal to nearly 5E−3, whereas ΔP_{ref2} is found to be negligible because $\Delta P_{D2} = 0$ puMW.

For a quantitative assessment of the obtained dynamic responses, numerical values of T_s, U_s, O_s and J regarding ΔF_1, ΔF_2 and ΔP_{tie} responses are calculated via Fig. 7 and reported in Table 3.

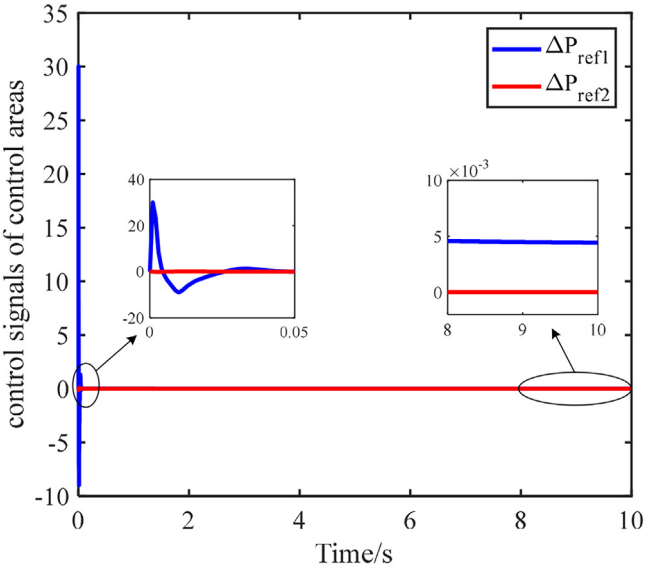

Fig. 8. Control signals of the TART PS under $\Delta P_{D1} = 0.01$ puMW.

As seen, the numerical results show the superior performance of SSA optimized F1PD-TI controller over the compared works in terms of smaller J (1.45E−9), shorter T_s ($\Delta F_1 = \Delta F_2 = \Delta Ptie = 0$ s), and less U_s ($\Delta F_1 = -0.0002$ Hz, $\Delta F_2 = -6.19E-6$ Hz, $\Delta Ptie = -2.17E-6$ puMW). Consequently, the results obtained for TART PS using the proposed approach improve the state-of-the-art sufficiently and thereby F1PD-TI controller is a competent one and able to contribute to the relevant literature.

To get a better picture of the frequency regulation, responses displaying the changes of power generations in area-1 ($\Delta P_{gArea-1}$) and area-2 ($\Delta P_{gArea-2}$) are presented in Fig. 9. It is apparent in Fig. 9(a) that the generated powers by STGs, WTGs, FCs, RESs, area-1 thermal are changed by $\Delta P_{gSTG} = 35.83E-4$ puMW, $\Delta P_{gWTG} = 59.92E-4$ puMW, $\Delta P_{gFC} = 1.29E-7$ puMW, $\Delta P_{gRES} = 57.46E-4$ puMW, $\Delta P_{gThermal} = 42.55E-4$ puMW, respectively. Thus, the total power generation change in area-1 is $\Delta P_{g1} = \Delta P_{gThermal} + \Delta P_{gRES} = 0.01$ puMW, which is equal to the change of power demand ΔP_{D1} applied to area-1. As a result, in response to the increase in load of PS by ΔP_{D1}, area-1 adjusts its power output as to be $\Delta P_{g1} = \Delta P_{D1}$ so that frequency regulation can be accomplished.

Similarly, the response of power change in area-2 is shown in Fig. 9(b). As there is no change in the demanded power of area-2, i.e. $\Delta P_{D2} = 0$ puMW, output power of area-2 does not change at steady-state, i.e. $\Delta P_{g2} = 0$ puMW. Nonetheless, since the area-2 is not a standalone power plant, but is interconnected with area-1, a change in area-1 affects the generation of area-2 transiently based on the interconnection strength.

4.2. MSTAHT PS

To reveal the efficacy and competence of the proposed control scheme in tackling different PSs, the research is forwarded to a more complex MSTAHT PS. By simulating this system with the optimized controller parameters in Table 2 under a SLD of $\Delta P_{D1} = 0.015$ puMW in area-1 at $t = 0$ s, the system dynamic responses are obtained and shown in Fig. 10. A comparison with the state-of-the-art variants such as GWO [6]/hFA-PS [7]/QODSA [8] tuned PID controller, BFOA tuned FPI/FPID [25] and ICA tuned FPIDN/C-I$^{\lambda}$D$^{\mu}$N [4] controllers is also established to recognize the contribution of the proposed approach. It is obvious from Fig. 10

Table 3
Comparative performance criteria values for TART PS.

Controller type	T_s(s)			$\|U_s\|$(Hz)		$\|U_s\|$(puMW)	$\|O_s\|$(Hz)		$\|O_s\|$(puMW)	J
	ΔF_1	ΔF_2	$\Delta Ptie$	ΔF_1	ΔF_2	$\Delta Ptie$	ΔF_1	ΔF_2	$\Delta Ptie$	
SOS: PIDN [13]	1.81	2.29	1.01	0.0036	0.00120	0.000471	3.56E−3	2.65E−3	9.15E−4	6.57E−6
BSO: FOPID [57]	0.83	1.41	1.05	0.0066	0.00287	0.000949	2.37E−4	**0**	**0**	1.76E−5
SCA: C-PDN-PIDN [16]	0.95	1.10	0.92	0.0023	0.00054	0.000334	8.92E−5	4.85E−5	2.30E−5	2.05E−6
hDE-PSO: FPID [29]	0.73	1.24	0.53	0.0034	0.00078	0.000313	**0**	**0**	**0**	2.57E−6
JA: FPIDN [31]	0.45	0.53	0.52	0.0016	0.00042	0.000180	**0**	**0**	**0**	7.44E−7
ICA: C-I^{2}D$^\mu$N [4]	0.04	0.21	0.22	0.0005	0.00007	0.000034	**0**	**0**	**0**	3.31E−8
SSA: F1PD-TI [studied]	**0**	**0**	**0**	**0.0002**	**6.19E−6**	**2.17E−6**	**6.85E−5**	**0**	**0**	**1.45E−9**

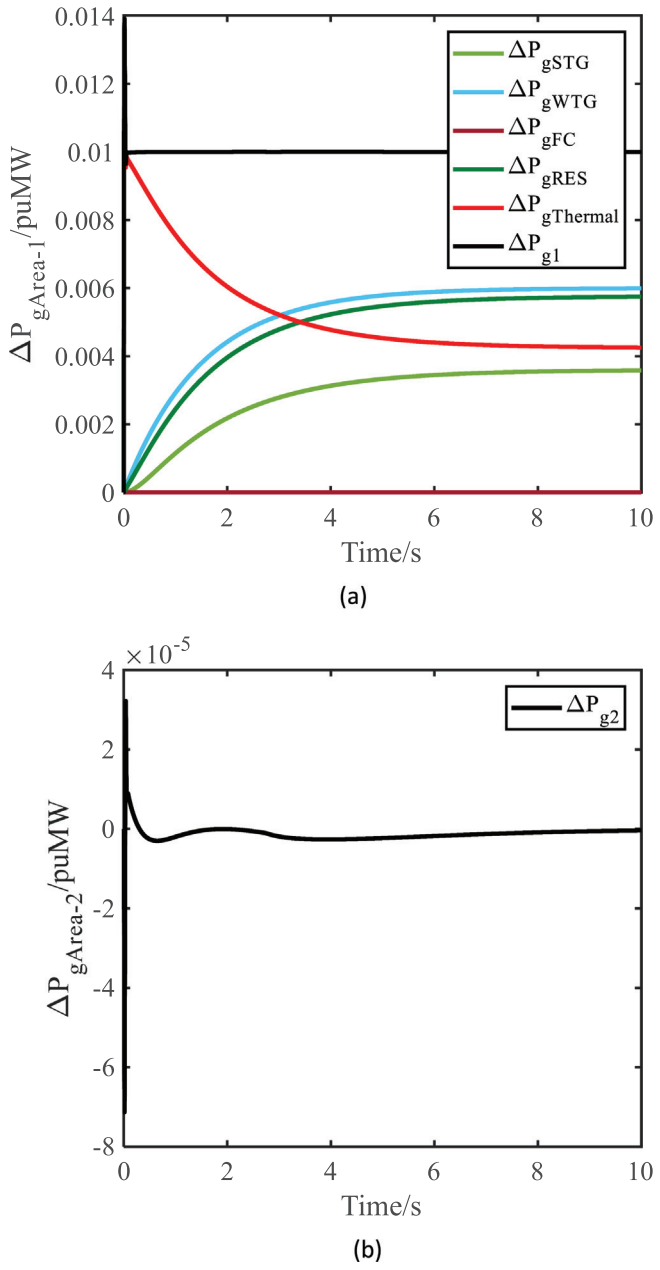

Fig. 9. Results of change in power generations for TART PS (a) $\Delta P_{gArea-1}$ (b).$\Delta P_{gArea-2}$

that the dynamic characteristics of ΔF_1, ΔF_2 and ΔP_{tie} responses for the proposed controller are significantly better than for other prevalent controllers recently appeared in the field. The responses obtained by the F1PD-TI controller deviate from their reference initially and then are recovered quickly with smaller overshoot and undershoot. This unveils that the proposed approach is capable to reject the given disturbance faster than other methods.

The respective controller signals in area-1 (ΔP_{ref1}) and area-2 (ΔP_{ref2}) are shown in Fig. 11. Similar to the conclusions drawn for Fig. 8, ΔP_{ref1} corresponding to $\Delta P_{D1} = 0.015$ puMW applied at $t = 0$ s presents some oscillations at transient-state and achieves the required steady-state value quickly. It is also noticeable that ΔP_{ref2} remains almost at zero because there is no demanded power in area-2, i.e. $\Delta P_{D2} = 0$ puMW.

Time-domain transient analysis of the obtained responses is also performed and the respective results are reported in Table 4. It is revealed from Table 4 that SSA optimized F1PD-TI controller outweighs all other approaches in terms of smaller J (5.98E−8), shorter T_s ($\Delta F_1 = 0.04$ s, $\Delta F_2 = \Delta Ptie = 0$ s), and less U_s ($\Delta F_1 = -0.0016$ Hz, $\Delta F_2 = -6.48E-5$ Hz, $\Delta Ptie = -1.99E-5$ puMW). As a result, the performance of the proposed method is affirmed in a more realistic MSTAHT PS by delivering superior results relative to several approaches in the literature.

The generation results in area-1 ($\Delta P_{gArea-1}$) and area-2 ($\Delta P_{gArea-2}$) are given in Fig. 12. As observed from Fig. 12(a), the changes in the generated powers by STGs, WTGs, FCs, RESs, area-1 thermal and area-1 hydro are $\Delta P_{gSTG} = 35.83E-4$ puMW, $\Delta P_{gWTG} = 59.92E-4$ puMW, $\Delta P_{gFC} = 1.29E-7$ puMW, $\Delta P_{gRES} = 57.46E-4$ puMW, $\Delta P_{gThermal-1} = 72.14E-4$ puMW, $\Delta P_{gHydro-1} = 20.42E-4$, respectively. This yields a total change in the area-1 power generation as $\Delta P_{g1} = \Delta P_{gThermal-1} + \Delta P_{gHydro-1} + \Delta P_{gRES} = 0.015$ puMW, which equals the demanded power change in area-1 ΔP_{D1}. Nonetheless, since the power demand does not change in area-2, i.e. $\Delta P_{D2} = 0$ puMW, the changes of power generations of both thermal and hydro units are zero, i.e. $\Delta P_{gThermal-2} = 0$ puMW, $\Delta P_{gHydro-2} = 0$ puMW as seen in Fig. 9(b). Thus, the total change in area-2 power generation is $\Delta P_{g2} = \Delta P_{gThermal-2} + \Delta P_{gHydro-2} = 0$ puMW that is also equal to ΔP_{D2}.

It is known that the power generations from STGs and WTGs are highly sensitive to environmental conditions such as wind speed (P_W) and solar irradiation (P_{sol}). In real-life, P_W and P_{sol} can be extremely unpredictable and variable depending on the atmospheric characteristics. Aiming at evaluating the controller performance in a more realistic case, wind speed and solar irradiation are hypothetically obtained as shown in Fig. 13(a) and this data is used in the MSTAHT PS. It can be clearly observed that P_W and P_{sol} fluctuate drastically and continuously over a period of 120 s to have the most challenging condition with regard to the RESs penetration. Using the same SLD and controller parameters in the previous experiment, i.e. those reported in Table 2, the corresponding ΔF_1, ΔF_2 and $\Delta Ptie$ responses are depicted in Fig. 13(b). Observe that the system stability is still maintained. After yielding large overshoots due to the RESs penetration initially, the responses are recovered quickly by the proposed approach. However, owing to the inconstant power generations from RESs, ΔF_1, ΔF_2 and $\Delta Ptie$ signals fluctuate around zero with a peak deviation of ± 0.005 Hz,

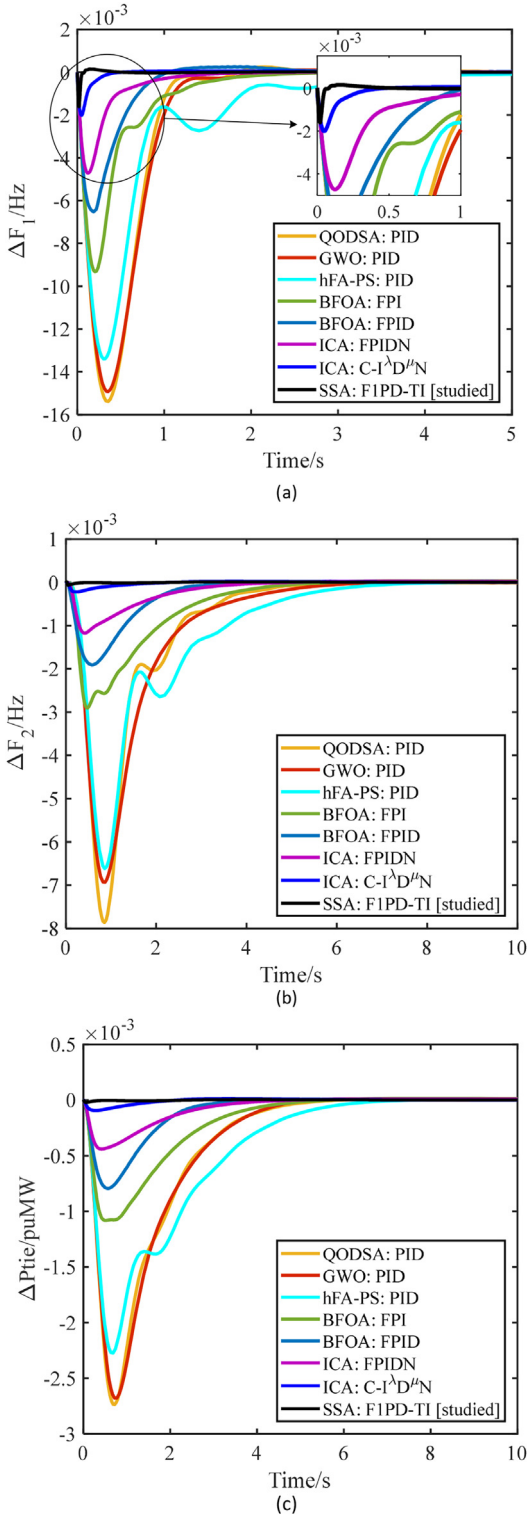

Fig. 10. Comparison of the MSTAHT PS responses under $\Delta P_{D1} = 0.015$ puMW (a) ΔF_1 (b) ΔF_2 (c).ΔP_{tie}

which is within the allowable range of frequency deviation as per the European grid regulations [56].

Moreover, the power generations given by ΔP_{gSTG}, ΔP_{gWTG}, ΔP_{gFC}, ΔP_{gRES}, $\Delta P_{gThermal-1}$ and $\Delta P_{gHydro-1}$ in area-1 present some oscillations in response to the variable P_W *and* P_{sol}. This yields a ΔP_{g1} to strictly track the demanded power $\Delta P_{D1} = 0.015$ puMW as seen from the zoomed view in Fig. 13(c). The responses of $\Delta P_{gThermal-2}$, $\Delta P_{gHydro-2}$

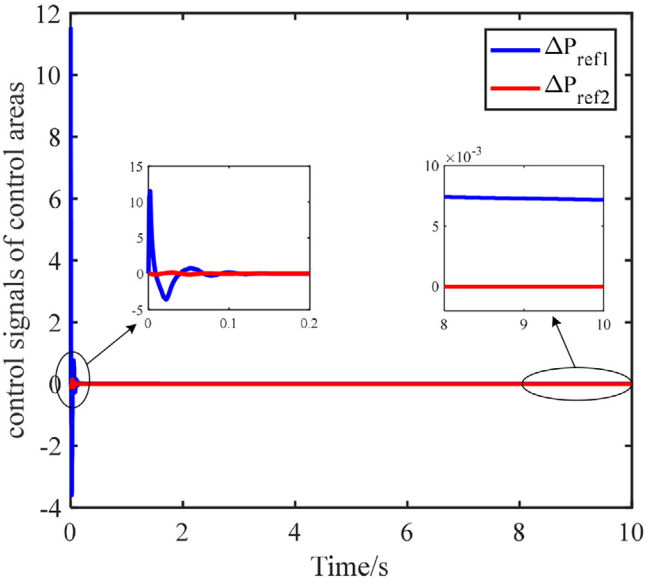

Fig. 11. Control signals of the MSTAHT PS under $\Delta P_{D1} = 0.015$ puMW.

and ΔP_{g2} obtained in area-2 keep closer to zero because there is no power demand in this area, i.e. $\Delta P_{D2} = 0$ puMW. These results justify the effectiveness and robustness of SSA optimized F1PD-TI controller in achieving a good level of controlling effort under RESs intermittency and volatility.

Everybody knows that renewable energy is good and clean for our planet which is being destroyed by the polluting greenhouse gases. However, too much of green energy causes problems for their supply. In principle, electrical energy, once generated, must be used instantly, and therefore we have to generate as much electricity as required at all times. In case of an excess energy during times of high penetration, i.e. for solar, during sunny days; for wind, during times of high wind speeds, it must be compensated somehow, otherwise it can lead to surges in frequency and tie-line power responses as shown in Fig. 13(b). One way of handling excess energy from RESs is to store it in different kinds of energy storage devices (ESDs). Given this, in order to increase grid flexibility and improve the integration of RESs, ESDs such as battery energy storage system (BESS) and flywheel energy storage system (FESS) are located in each area of MSTAHT PS as seen in Fig. 1(b). Observe that the output of ESDs, ΔP_{gESD}, is controlled by the ACE signal and the output is connected to the summing point with a minus sign. Due to the swift energy storing action of BESS and FESS, they can represented by the following first-order TF models.

$$G_{BESS}(s) = \frac{K_{bess}}{sT_{bess} + 1} \tag{9}$$

$$G_{FESS}(s) = \frac{K_{fess}}{sT_{fess} + 1} \tag{10}$$

where K_{bess} and K_{fess} are the gains and T_{bess} and T_{fess} are the time constants of BESS and FESS, respectively. It is supposed that the intermittency in wind speed, solar irradiation and even load disturbance are cancelled out by the inclusion of the respective ESDs. If the power plant faces a surplus power from RESs, ESDs will store it and release it later back to the plant when the power generated is less than the demand. In this way, ESDs can play an important role as backup energy sources in damping frequency and tie-line power fluctuations in the face of RESs uncertainty and load variation.

Table 4
Comparative performance criteria values for MSTAHT PS.

Controller type	T_s(s)			$\|U_s\|$(Hz)		$\|U_s\|$(puMW)	$\|O_s\|$(Hz)		$\|O_s\|$(puMW)	J
	ΔF_1	ΔF_2	$\Delta Ptie$	ΔF_1	ΔF_2	$\Delta Ptie$	ΔF_1	ΔF_2	$\Delta Ptie$	
QODSA: PID [8]	1.10	3.36	2.57	0.0154	0.0078	0.00274	2.50E−4	**0**	**0**	1.50E−4
GWO: PID [6]	1.21	3.50	2.64	0.0149	0.0069	0.00260	**0**	**0**	**0**	1.47E−4
hFA-PS: PID [7]	2.94	4.53	3.30	0.0134	0.0066	0.00220	**0**	**0**	**0**	1.17E−4
BFOA: FPI [25]	1.41	2.86	1.92	0.0093	0.0029	0.00108	**0**	**0**	**0**	1.60E−5
BFOA: FPID [25]	0.82	1.79	1.17	0.0065	0.0019	0.00079	2.59E−4	**0**	**0**	1.60E−5
ICA: FPIDN [4]	0.78	1.59	0.60	0.0047	0.0011	0.00043	**0**	**0**	**0**	6.01E−6
ICA: C-$I^{\lambda}D^{\mu}$N [4]	0.18	0.21	0.27	0.0020	0.0002	0.00009	**0**	**0**	**0**	3.68E−7
SSA: F1PD-TI [studied]	**0.04**	**0**	**0**	**0.0016**	**6.48E−5**	**1.99E−5**	**1.45E−4**	**0**	**0**	**5.98E−8**

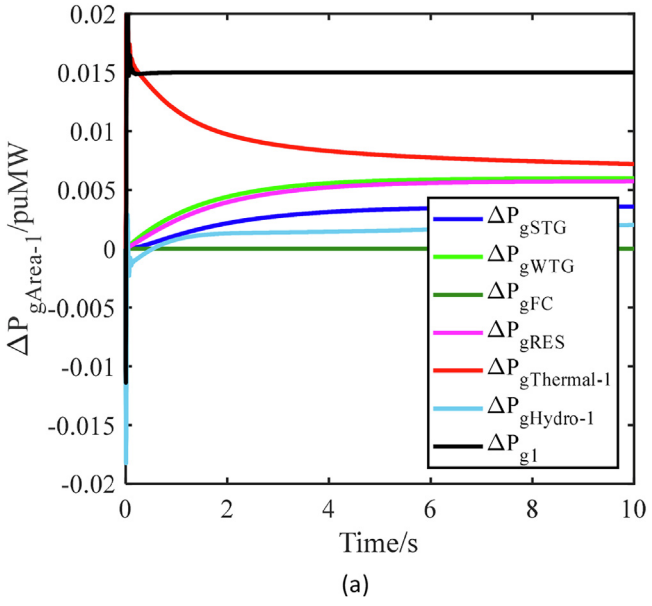

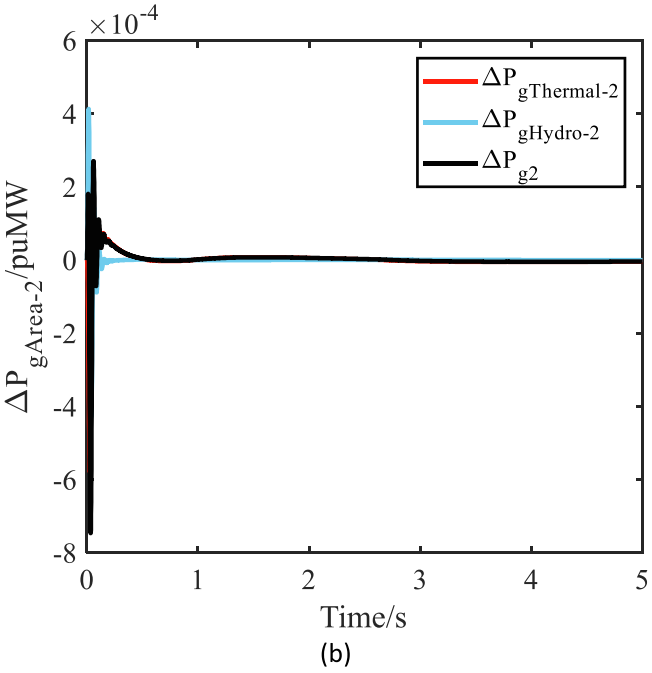

Fig. 12. Results of change in power generations for MSTAHT PS (a) $\Delta P_{gArea-1}$ (b).$\Delta P_{gArea-2}$

Fig. 14 shows the ΔF_1, ΔF_2, ΔP_{tie} signals when the ESDs are included in the MSTAHT PS having inconstant generation from RESs as in the previous case. To highlight the efficacy of the employed ESDs on the system performance, previous results without ESDs, i.e. those seen in Fig. 13(b) are also presented in Fig. 14. It is clearly noticeable from Fig. 14 that the results obtained with ESDs are significantly better than those without ESDs, where the frequency and tie-line power fluctuations are suppressed effectively. This is attributed to the fact that the BESS and FESS serve as reserving units, storing surplus power during the time generation exceeds the demand and releasing the energy stored previously to the power plant when the demand exceeds generation. Consequently, ESDs can assist the system in preserving its generation and demand balance and they are favorable to deal effectively with the uncertain energy from RESs.

4.3. Nonlinear effects of governor dead band and generation rate constraint

Nonlinearity sources in PSs such as governor dead band (GDB) and generation rate constraint (GRC) are employed in this section to show the performance of F1PD-TI controller against nonlinearities. For this exercise, TART PS is used as test system.

GDB presents oscillations within the system as there are a number of speed variations in which the valve position owing to the impact of GDB does not vary [36]. To analyze the dynamics of GDB nonlinearity, the governor TF model seen in Fig. 1(a) is replaced by the following model, where $T_g = 0.2$ s.

$$G_s(s) = \frac{-(0.2/\pi)s + 0.8}{sT_g + 1} \tag{11}$$

Another significant source of nonlinearity in PSs is introduced by the generation rate constraint (GRC). GRC corresponds to the limitations of thermal and mechanical processes, which require some finite time to be completed. As its name implies, GRC is a constraint that limits the rate of change of the power generation and therefore it enables the generated power to change at a definite rate only [11]. As such, GRC is an indispensable means for a realistic research on AGC. The common open loop model of GRC depicted in Fig. 15 is employed in thermal turbines of TART PS. $\pm\delta$ seen in Fig. 15 is an adjustable parameter standing for the limits of GRC.

GDB and GRC are individually considered in TART PS and the SSA based optimization process described before is repeated to find out the optimal controller parameters that accommodate the new condition. In the study, the consequence of different GRC limits on the system performance is also explored. In this context, δ is set to ±0.02 puMW/s, ±0.0033 puMW/s and ±0.002 puMW/s, respectively. The final controller parameters and the respective J values are provided in Table 5. Decreasing trend of the J signifies a deterioration in the system performance.

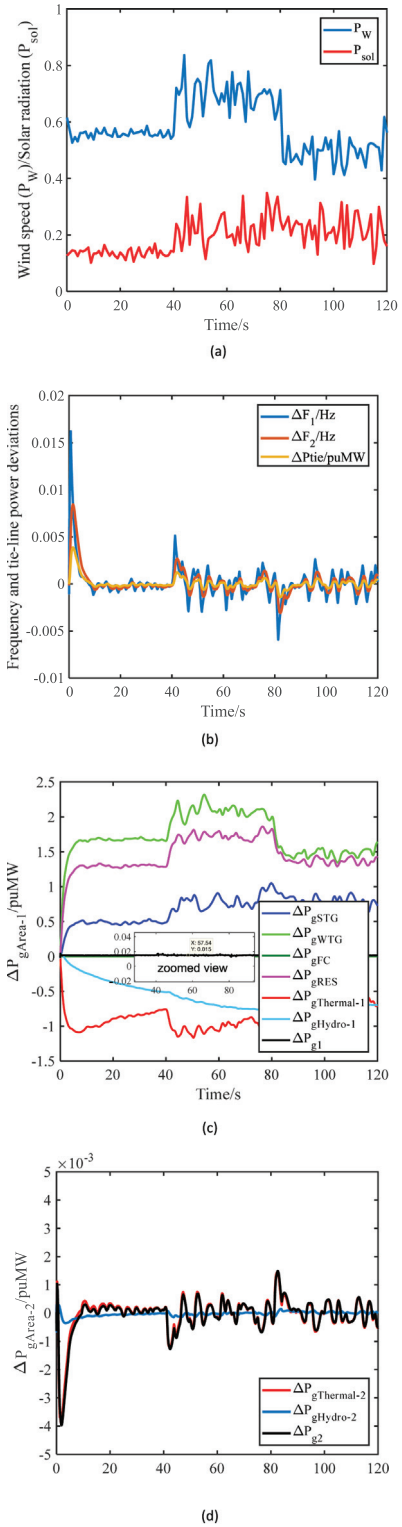

Fig. 13. Results of MSTAHT PS in presence of solar irradiation and wind speed changing abruptly (a) P_W/P_{sol} (b) ΔF_1, ΔF_2 and $\Delta Ptie$ (c) $\Delta P_{gArea-1}$ (d).$\Delta P_{gArea-2}$

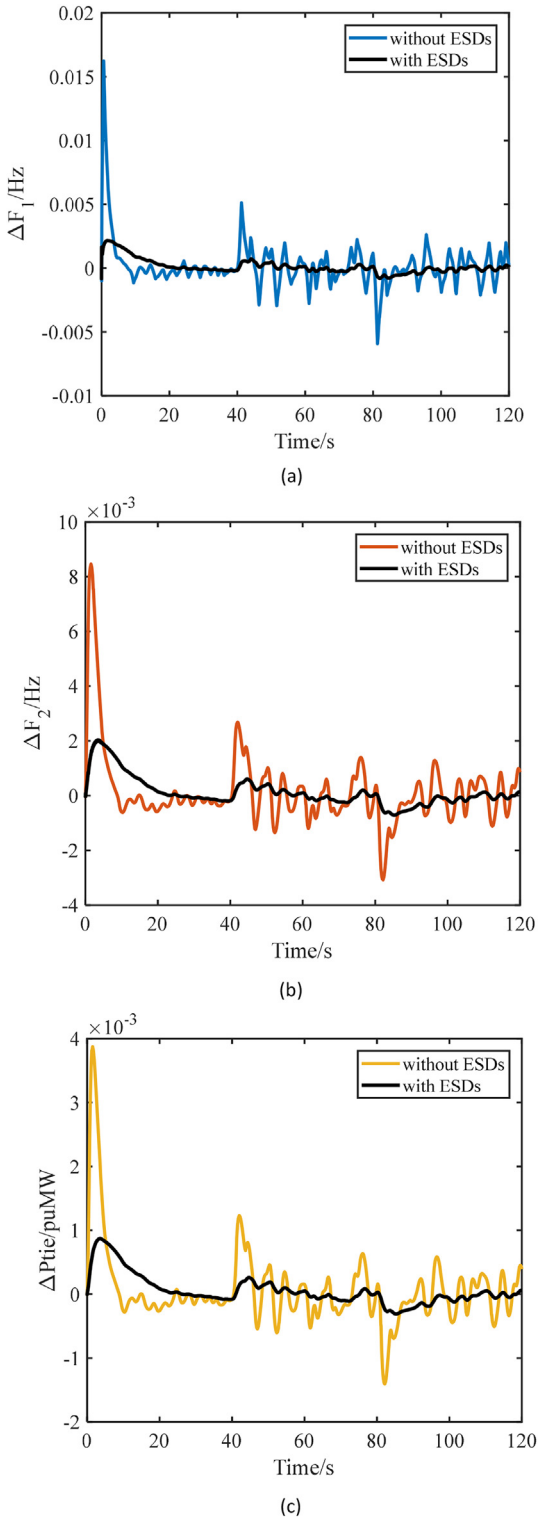

Fig. 14. Comparison of the results with and without ESDs under RESs intermittency and volatility (a) ΔF_1 (b) ΔF_2 (c).$\Delta Ptie$

The dynamic responses of the nonlinear TART PS in presence of GDB and GRC are displayed in Fig. 16. For comparison, the nominal response is also presented in this figure. It is apparent that larger deviations in $T_s/O_s/U_s$ are introduced by the incorporation of GDB and GRC comparing with the nominal case. However, after some undershoot and overshoot, ΔF_1, ΔF_2 and ΔP_{tie} responses in the system reach back their desired steady-state value. This con-

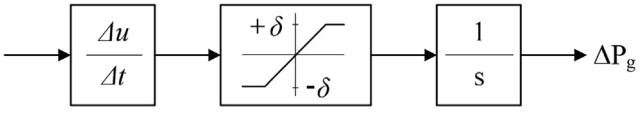

Fig. 15. Open loop model of GRC.

Table 5
Optimized controller parameters under GDB and GRC nonlinearities.

Controllers parameters	Nonlinear TART PS			
	GDB	GRC of ± 0.02	GRC of ± 0.0033	GRC of ± 0.002
K_p	0.0001	4.1765	1.0349	2.9694
K_d	0.2364	0.0046	0.7057	1.7978
K_t	0.4461	3.2247	1.6268	0
K_i	0.4255	4.0825	3.5225	0.1837
K_1	9.9999	9.9998	1.3482	0
K_2	7.6996	2.4732	0.9612	0
n	0.1925	0.0100	0.0100	0.2500
J	9.89E−6	7.64E−5	1.89E−3	4.23E−3

firms that F1PD-TI controller is able to deal with the incorporated nonlinearities sufficiently without loss of system stability. It is disclosed that if the GRC limit is reduced, the dynamic characteristics of the PS are worsen considerably. It is also worth noting that the proposed approach can control the system effectively with its integral component only when the GRC limit is set to ±0.002 because K_1, K_2 and K_t are found to be zero in such a case.

4.4. Influence of membership functions shape on the system performance

Eventually, influence of MFs shape on the system performance under study is explored. For comparison, trapezoidal, generalized bell-shaped and gaussian MFs shown in Fig. 17 are designed and their performances are contrasted by that of the triangular MF in Fig. 4 by using the TART PS as test system.

To adapt the F1PD-TI controller to different shapes of MFs, its parameters are re-tuned by the SSA concept for each case, which are reported in Table 6 along with the associated J value. Note that controller parameters for the triangular MF have been already presented in Table 2.

The system outcomes acquired for each shape of the MFs are displayed in Fig. 18. As we can see, the frequency regulation is deteriorated by trapezoidal MF, which causes sustained oscillations with low magnitude in ΔF_1, ΔF_2 and ΔP_{tie} responses. The performance of generalized bell-shaped MF is better than that of the trapezoidal shape, but lower than that of the gaussian shape. Since the triangular and gaussian are similar to each other in shape, they result in more or less similar level of performance. Among the MFs compared, triangular MF is found to be the best shape yielding the least deviations for ΔF_1, ΔF_2 and ΔP_{tie} signals, which is followed by gaussian, generalized bell-shaped and trapezoidal MFs, respectively. This justifies the use of triangular MF in this work.

5. Conclusions

A novel F1PD-TI controller is presented in this paper for AGC of PSs with renewable power penetration and energy storage devices. The controller configuration that we propose comprises F1PD controller and TI controller connected in cascade. Based on our knowledge, it seems there is no previous research similar to the proposed control scheme. To ensure more effective performance of the proposed controller, its seven parameters are optimized by taking advantages of SSA concept. The resulting controller provides a simple and efficient control strategy for frequency regulation in different PSs. Performance achieved is checked through a TART PS and a MSTAHT PS, which are integrated with renewable generations based on solar thermal, wind and fuel cells. A thorough comparison with the latest variants is also presented to show the dominance and contribution of the proposed approach. It is found that SSA optimized F1PD-TI controller outweighs all its competing peers by rendering minimum $T_s/U_s/O_s$ values regarding ΔF_1, ΔF_2 and ΔP_{tie} signals. The performance of F1PD-TI controller is also verified under RESs intermittency and volatility, where wind speed and solar irradiation change as in a realistic condition. ESDs are applied to deal better with the surplus power from the RESs, and they are shown to be effective units in improving the system dynamic responses by storing and delivering energy when the generation does not match with the demand. Moreover, nonlinearities resulting from the physical constraints such as GDB and GRC are considered one at time in the system. Although the occurrence of GDB and GRC results in some performance degradation, F1PD-TI controller is shown able to cope with the nonlinearities satisfactorily by preserving system stability. Consequently, with higher GRC value, better responses with shorter settling time and smaller undershoot/overshoot are observed. At the end of the work, the supreme performance of the used triangular MF over other popular shapes is justified. Besides, SSA is shown to be better than some popular algorithms in achieving more accurate solutions for the problems at hand.

As revealed by the above analysis, results and discussion, the proposed SSA optimized F1PD-TI controller may also be a powerful controller in other PSs and control application areas. This entails further investigation. Optimization of fuzzy membership function parameters is also worthy of studying. Applying newer metaheuristic algorithms to the same problem for a comparison with SSA could be beneficial.

Declaration of Competing Interest

The authors declare that they have no known competing financial interests or personal relationships that could have appeared to influence the work reported in this paper.

Appendix 1. Justification for the selection of SSA

To justify the selection of SSA as the optimizer in the current study, a comparative study is established by applying some well-regarded algorithms such as particle swarm optimization (PSO), gravitation search algorithm (GSA), artificial bee colony (ABC) algorithm, flower pollination algorithm (FPA), gray wolf optimizer (GWO) and moth-flame optimization (MFO) to the controller parameters' optimization for TART PS and MSTAHT PS. For the fairness of comparison, number of fitness function evaluations is set to 5000 for all algorithms.

Two performance criteria are employed to quantify the overall performance of SSA against other indicated algorithms. These are average and standard deviation (std) of the best results found after 30 independent runs. The former metric indicates how SSA performs in average while the latter one shows the algorithm robustness over all the runs. Moreover, the non-parametric Wilcoxon rank-sum test is applied at the 5% level of significance in order to test the performance of each run individually and show whether the results obtained by SSA are significant.

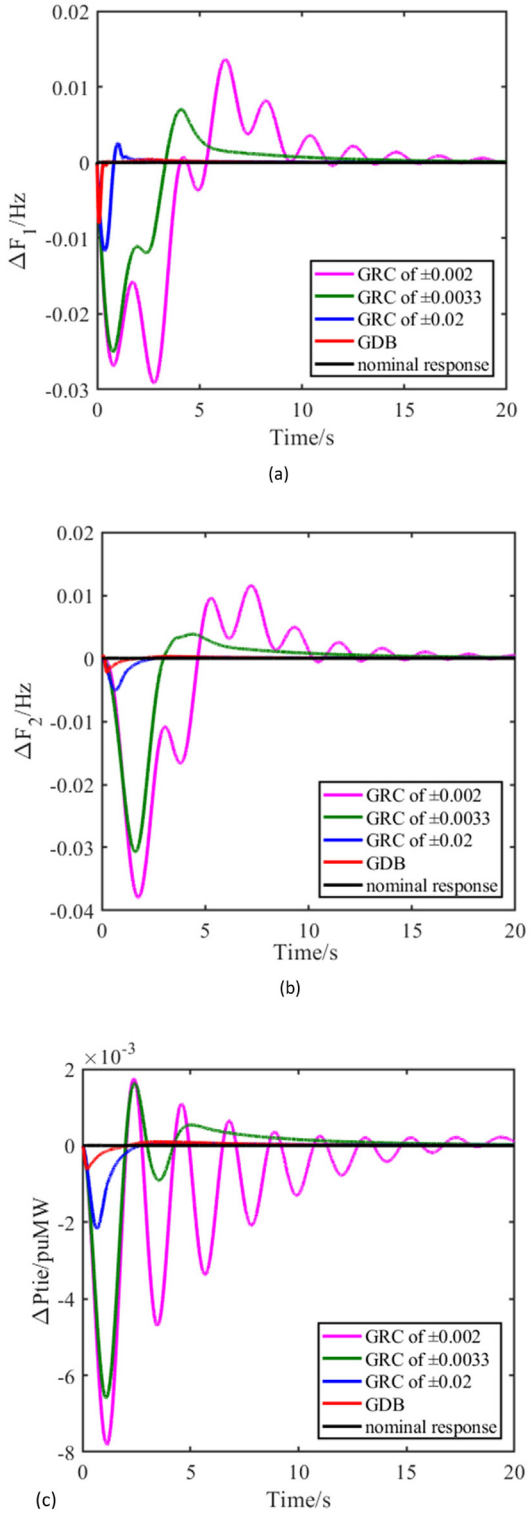

Fig. 16. Comparison of the nonlinear TART PS responses under GDB and GRC nonlinearities (a) ΔF_1 (b) ΔF_2 (c).ΔP_{tie}

The results for the cost function (J) minimization are provided in Table 7, where comparatively the best results are bolded. In the Wilcoxon rank-sum test, the best algorithm is selected and compared with others independently. Given an example, if SSA is the best algorithm, the pairwise comparison is made between SSA/PSO, SSA/GSA and so on. p-values that are smaller than 0.05 signify that the obtained results are significant while those greater than 0.05 (underlined) indicate that the algorithms in the pairwise comparison have identical performance. Since the best algorithm could not be compared with itself, its associated p-value is presented as n/a (not applicable).

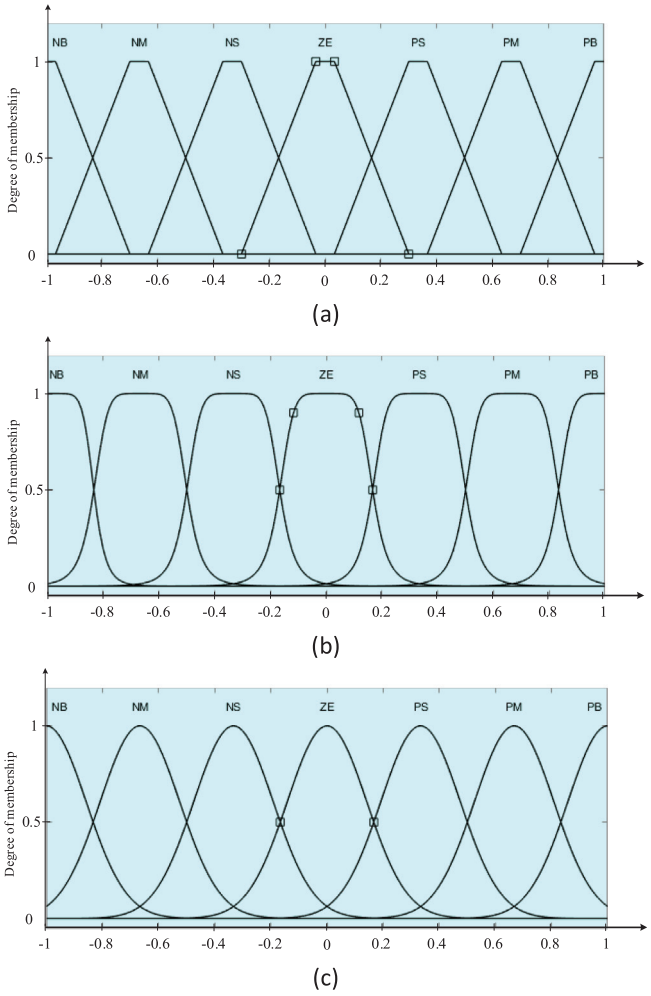

Fig. 17. Shapes of MFs (a) trapezoidal (b) generalized bell-shaped (c) Gaussian.

Table 6
Optimized controller parameters for different shapes of MFs.

Controllers parameters	Shapes of MFs		
	trapezoidal	Generalized bell-shaped	Gaussian
K_p	2.0516	2.4998	3.7542
K_d	0.0101	4.9999	0.1987
K_t	5.0000	3.7882	4.8087
K_i	3.2583	2.2937	3.9768
K_1	7.5060	7.7114	6.5877
K_2	9.9999	0.1982	2.2665
n	0.0293	0.0851	0.1759
J	3.37E−6	4.42E−7	6.46E−8

According to the results in Table 7, SSA has the best performance for TART PS. However, p-values disclose that SSA does not provide superior results compared to MFO. Thus, SSA and MFO are the best algorithms for TART PS. The results for MSTAHT PS show that SSA has the highest performance in terms of the results of average and std. In addition, the respective p-values are all below 0.05, verifying that the superiorities of SSA are significant. As a result, these numerical findings, as well as simplicity and low computation demand of SSA are the main reasons for the choice of SSA as optimizer in the current study.

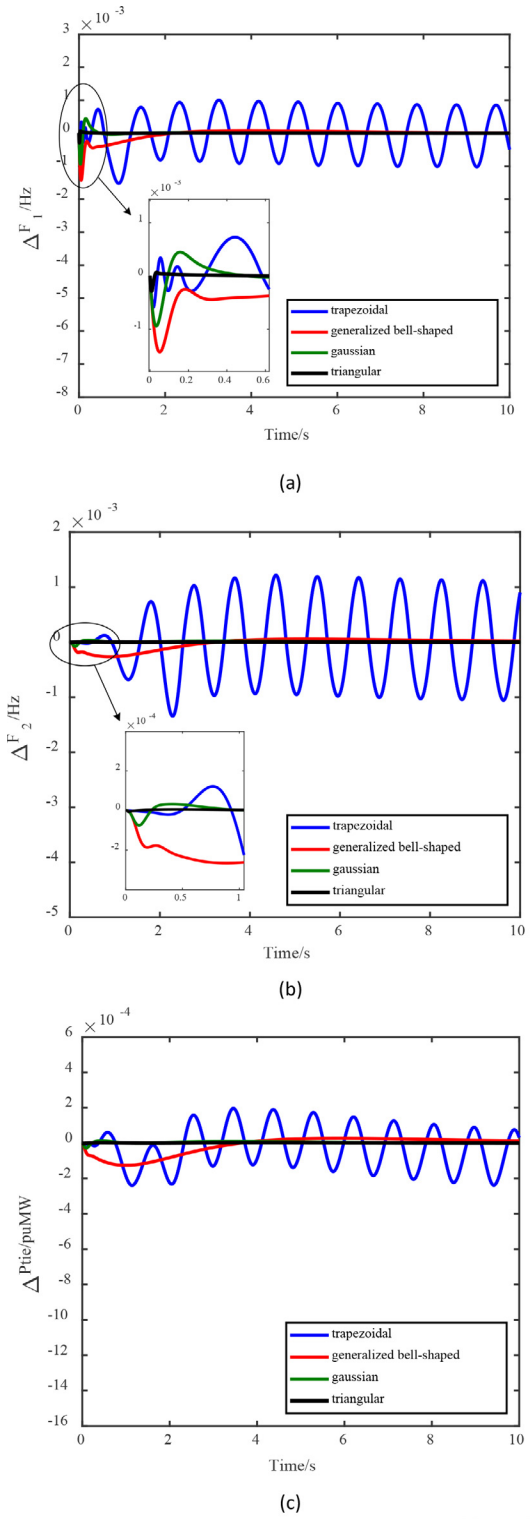

Fig. 18. Results of TART PS under different shapes of MFs (a) ΔF_1 (b) ΔF_2 (c).ΔP_{tie}

Appendix 2. System data

Nominal parameters of two-area RTS [4]

$P_r = 2000$ MW, $T_{ps} = 20$ s, $K_{ps} = 120$ Hz/puMW, $T_g = 0.08$ s, $T_t = 0.3$ s, $K_r = 0.5$, $T_r = 10$ s, $2\pi T_{12} = 0.545$ puMW/Hz, $B = 0.425$ puMW/Hz, $R = 2.4$ Hz/puMW, $F^0 = 60$ Hz.

Nominal parameters of two-area MSHTS [4]

$P_r = 2000$ MW, $T_{ps} = 20$ s, $K_{ps} = 100$ Hz/puMW, $T_g = 0.08$ s, $T_t = 0.3$ s,$T_{rh} = 48.7$ s, $T_R = 5$ s, $T_{gh} = 0.513$ s, $T_w = 1$ s, $T_{12} = 0.0707$ puMW/Hz, $B = 0.425$ puMW/Hz, $R_1 = 2$ Hz/puMW, $R_2 = 2.4$ Hz/puMW, $F^0 = 60$ Hz.

Nominal parameters of RESs [4]

$T_s = 1.8$ s, $K_s = 1.8$, $T_T = 0.3$ s, $K_t = 1$, $T_{wtg} = 1.5$ s, $K_{wtg} = 1$, $K_n = 0.6$, $T_{ae} = 0.5$ s, $K_{ae} = 0.002$ $T_{fc} = 4$ s,.$K_{fc} = 0.01$

Nominal parameters of ESDs

$T_{bess} = 1.8$ s, $K_{bess} = -3$, $T_{fess} = 0.3$ s,.$K_{fess} = -1.5$

Appendix 3. State-space modelling

This section is devoted to derive the state-space models of the studied PSs in the following form:

$$\begin{aligned} \dot{X} &= AX + BU + \Gamma Q \\ Y &= CX \end{aligned} \tag{12}$$

Here X, U, Q and Y represent state, input, disturbance and output matrices respectively whereas A, B, Γ and C are system, input distribution, disturbance distribution and output distribution matrices respectively. Note that all the symbols used for the modelling are shown in Fig. 1. For TART PS with RES penetration, nine first-order differential equations are acquired and the system is represented using nine state variables. Choosing ΔF_1, ΔF_2 and $\Delta Ptie$ as outputs, the arrangements of X, A, B, Γ, U, Q and C can be presented as follows:

$$X = \left[\Delta F_1 \Delta F_2 \Delta Ptie \Delta X_{g1} \Delta X_{g2} \Delta X_{rh1} \Delta X_{rh2} \Delta X_{t1} \Delta X_{t2}\right]^T$$

$$A = \begin{bmatrix} -\frac{1}{T_{ps}} & 0 & -\frac{K_{ps}}{T_{ps}} & 0 & 0 & 0 & 0 & \frac{K_{ps}}{T_{ps}} & 0 \\ 0 & -\frac{1}{T_{ps}} & \frac{K_{ps}}{T_{ps}} & 0 & 0 & 0 & 0 & 0 & \frac{K_{ps}}{T_{ps}} \\ 2\pi T_{12} & -2\pi T_{12} & 0 & 0 & 0 & 0 & 0 & 0 & 0 \\ -\frac{1}{RT_g} & 0 & 0 & -\frac{1}{T_g} & 0 & 0 & 0 & 0 & 0 \\ 0 & -\frac{1}{RT_g} & 0 & 0 & -\frac{1}{T_g} & 0 & 0 & 0 & 0 \\ -\frac{K_r T_r}{RT_g T_r} & 0 & 0 & -\frac{K_r T_r}{T_g T_r} & 0 & -\frac{1}{T_r} & 0 & 0 & 0 \\ 0 & -\frac{K_r T_r}{RT_g T_r} & 0 & 0 & -\frac{K_r T_r}{T_g T_r} & 0 & -\frac{1}{T_r} & 0 & 0 \\ 0 & 0 & 0 & 0 & 0 & \frac{1}{T_t} & 0 & -\frac{1}{T_t} & 0 \\ 0 & 0 & 0 & 0 & 0 & 0 & \frac{1}{T_t} & 0 & -\frac{1}{T_t} \end{bmatrix}$$

$$B = \begin{bmatrix} 0 & 0 \\ 0 & 0 \\ 0 & 0 \\ \frac{1}{T_g} & 0 \\ 0 & \frac{1}{T_g} \\ \frac{K_r T_r}{T_g T_r} & 0 \\ 0 & \frac{K_r T_r}{T_g T_r} \\ 0 & 0 \\ 0 & 0 \end{bmatrix}, \Gamma = \begin{bmatrix} -\frac{K_{ps}}{T_{ps}} & 0 & \frac{K_{ps}}{T_{ps}} \\ 0 & -\frac{K_{ps}}{T_{ps}} & 0 \\ 0 & 0 & 0 \\ 0 & 0 & 0 \\ 0 & 0 & 0 \\ 0 & 0 & 0 \\ 0 & 0 & 0 \\ 0 & 0 & 0 \\ 0 & 0 & 0 \end{bmatrix}$$

$$U = \left[\Delta P_{ref1}\ \Delta P_{ref2}\right]^T,\ Q = \left[\Delta P_{D1}\ \Delta P_{D2}\ \Delta P_{gRES}\right]^T$$

$$C = \begin{bmatrix} 1 & 0 & 0 & 0 & 0 & 0 & 0 & 0 & 0 \\ 0 & 1 & 0 & 0 & 0 & 0 & 0 & 0 & 0 \\ 0 & 0 & 1 & 0 & 0 & 0 & 0 & 0 & 0 \end{bmatrix}$$

Table 7
Minimization results of J for different algorithms.

Algorithms	TART PS			MSTAHT PS		
	Average	Std	p-values	Average	Std	p-values
PSO	2.33E−7	3.30E−7	7.41E−4	4.24E−7	3.71E−7	7.96E−5
GSA	8.01E−8	2.10E−8	1.76E−4	4.12E−7	3.16E−7	7.96E−5
ABC	3.15E−7	3.36E−7	4.28E−4	4.20E−7	3.33E−7	0.0013
FPA	2.70E−7	2.89E−7	5.69E−4	3.71E−7	3.23E−7	0.0013
GWO	4.88E−8	3.30E−8	0.0024	1.94E−7	2.38E−7	7.96E−5
MFO	9.93E−9	1.66E−8	0.3438	7.79E−8	1.35E−8	6.18E−4
SSA	**5.68E−9**	**6.63E−9**	**n/a**	**6.07E−8**	**1.62E−9**	**n/a**

In order to obtain the state-space model of MSTAHT PS, ESDs are also taken into account. Fifteen first-order differential equations are written and the arrangements of X, A, B, Γ, U, Q and C for the fifteen state variables are derived as:

$$X = \left[\Delta F_1 \Delta F_2 \Delta Ptie \Delta X_{g1} \Delta X_{g2} \Delta X_{rh1} \Delta X_{rh2} \Delta X_{h1} \Delta X_{h2} \Delta P_{gThermal-1} \Delta P_{gThermal-2} \Delta P_{gHydro-1} \Delta P_{gHydro-2} \Delta P_{gESD1} \Delta P_{gESD2}\right]^T$$

$$A = \begin{bmatrix}
-\frac{1}{T_{ps}} & 0 & -\frac{K_{ps}}{T_{ps}} & 0 & 0 & 0 & 0 & 0 & 0 & \frac{K_{ps}}{T_{ps}} & 0 & \frac{K_{ps}}{T_{ps}} & 0 & -\frac{K_{ps}}{T_{ps}} & 0 \\
0 & -\frac{1}{T_{ps}} & \frac{K_{ps}}{T_{ps}} & 0 & 0 & 0 & 0 & 0 & 0 & 0 & \frac{K_{ps}}{T_{ps}} & 0 & \frac{K_{ps}}{T_{ps}} & 0 & -\frac{K_{ps}}{T_{ps}} \\
2\pi T_{12} & -2\pi T_{12} & 0 & 0 & 0 & 0 & 0 & 0 & 0 & 0 & 0 & 0 & 0 & 0 & 0 \\
-\frac{1}{R_1 T_g} & 0 & 0 & -\frac{1}{T_g} & 0 & 0 & 0 & 0 & 0 & 0 & 0 & 0 & 0 & 0 & 0 \\
0 & -\frac{1}{R_1 T_g} & 0 & 0 & -\frac{1}{T_g} & 0 & 0 & 0 & 0 & 0 & 0 & 0 & 0 & 0 & 0 \\
-\frac{1}{R_2 T_{rh}} & 0 & 0 & 0 & 0 & -\frac{1}{T_{rh}} & 0 & 0 & 0 & 0 & 0 & 0 & 0 & 0 & 0 \\
0 & -\frac{1}{R_2 T_{rh}} & 0 & 0 & 0 & 0 & -\frac{1}{T_{rh}} & 0 & 0 & 0 & 0 & 0 & 0 & 0 & 0 \\
-\frac{T_R}{R_2 T_{gh} T_{rh}} & 0 & 0 & 0 & 0 & \frac{T_{rh}-T_R}{T_{rh}} & 0 & -\frac{1}{T_{gh}} & 0 & 0 & 0 & 0 & 0 & 0 & 0 \\
0 & -\frac{T_R}{R_2 T_{gh} T_{rh}} & 0 & 0 & 0 & 0 & \frac{T_{rh}-T_R}{T_{rh}} & 0 & -\frac{1}{T_{gh}} & 0 & 0 & 0 & 0 & 0 & 0 \\
0 & 0 & 0 & \frac{1}{T_t} & 0 & 0 & 0 & 0 & 0 & -\frac{1}{T_t} & 0 & 0 & 0 & 0 & 0 \\
0 & 0 & 0 & 0 & \frac{1}{T_t} & 0 & 0 & 0 & 0 & 0 & -\frac{1}{T_t} & 0 & 0 & 0 & 0 \\
\frac{T_R}{0.5 R_2 T_{gh} T_{rh}} & 0 & 0 & 0 & 0 & \frac{T_R-T_{rh}}{0.5 T_{gh} T_{rh}} & 0 & \frac{T_{gh}+T_w}{0.5 T_w T_{gh}} & 0 & 0 & 0 & -\frac{1}{0.5 T_w} & 0 & 0 & 0 \\
0 & \frac{T_R}{0.5 R_2 T_{gh} T_{rh}} & 0 & 0 & 0 & 0 & \frac{T_R-T_{rh}}{0.5 T_{gh} T_{rh}} & 0 & \frac{T_{gh}+T_w}{0.5 T_w T_{gh}} & 0 & 0 & 0 & -\frac{1}{0.5 T_w} & 0 & 0 \\
-\frac{BK_{esd}}{T_{esd}} & 0 & -\frac{K_{esd}}{T_{esd}} & 0 & 0 & 0 & 0 & 0 & 0 & 0 & 0 & 0 & 0 & -\frac{1}{T_{esd}} & 0 \\
0 & -\frac{BK_{esd}}{T_{esd}} & \frac{K_{esd}}{T_{esd}} & 0 & 0 & 0 & 0 & 0 & 0 & 0 & 0 & 0 & 0 & 0 & -\frac{1}{T_{esd}}
\end{bmatrix}$$

$$B = \begin{bmatrix}
0 & 0 \\ 0 & 0 \\ 0 & 0 \\ \frac{1}{T_g} & 0 \\ 0 & \frac{1}{T_g} \\ \frac{1}{T_{rh}} & 0 \\ 0 & \frac{1}{T_{rh}} \\ \frac{T_R}{T_{gh} T_{rh}} & 0 \\ 0 & \frac{T_R}{T_{gh} T_{rh}} \\ 0 & 0 \\ 0 & 0 \\ -\frac{T_R}{0.5 T_{gh} T_{rh}} & 0 \\ 0 & -\frac{T_R}{0.5 T_{gh} T_{rh}} \\ 0 & 0 \\ 0 & 0
\end{bmatrix}, \Gamma = \begin{bmatrix}
-\frac{K_{ps}}{T_{ps}} & 0 & \frac{K_{ps}}{T_{ps}} \\ 0 & -\frac{K_{ps}}{T_{ps}} & 0 \\ 0 & 0 & 0 \\ 0 & 0 & 0 \\ 0 & 0 & 0 \\ 0 & 0 & 0 \\ 0 & 0 & 0 \\ 0 & 0 & 0 \\ 0 & 0 & 0 \\ 0 & 0 & 0 \\ 0 & 0 & 0 \\ 0 & 0 & 0 \\ 0 & 0 & 0 \\ 0 & 0 & 0
\end{bmatrix}$$

$$U = \left[\Delta P_{ref1} \Delta P_{ref2}\right]^T, Q = \left[\Delta P_{D1} \Delta P_{D2} \Delta P_{gRES}\right]^T$$

$$C = \begin{bmatrix}
1 & 0 & 0 & 0 & 0 & 0 & 0 & 0 & 0 & 0 & 0 & 0 & 0 & 0 & 0 \\
0 & 1 & 0 & 0 & 0 & 0 & 0 & 0 & 0 & 0 & 0 & 0 & 0 & 0 & 0 \\
0 & 0 & 1 & 0 & 0 & 0 & 0 & 0 & 0 & 0 & 0 & 0 & 0 & 0 & 0
\end{bmatrix}$$

References

[1] A. Rahman, L.C. Saikia, N. Sinha, AGC of dish-Stirling solar thermal integrated thermal system with biogeography based optimised three degree of freedom PID controller, IET Renew. Power Gener. 10 (8) (2016) 1161–1170.
[2] D. Kler, V. Kumar, K.P.S. Rana, Optimal integral minus proportional derivative controller design by evolutionary algorithm for thermal-renewable energy-hybrid power systems, IET Renew. Power Gener. 13 (11) (2019) 2000–2012.
[3] D.C. Das, A.K. Roy, N. Sinha, GA based frequency controller for solar thermal-diesel-wind hybrid energy generation/energy storage system, Int. J. Electr. Power Energy Syst. 43 (1) (2012) 262–279.
[4] Y. Arya, N. Kumar, P. Dahiya, G. Sharma, E. Çelik, S. Dhundhara, M. Sharma, Cascade-IλDμN controller design for AGC of thermal and hydrothermal power systems integrated with renewable energy sources, IET Renew. Power Gener. 15 (3) (2021) 504–520.
[5] J. Nanda, M. Sreedhar, A. Dasgupta, A new technique in hydro thermal interconnected automatic generation control system by using minority charge carrier inspired algorithm, Int. J. Electr. Power Energy Syst. 68 (2015) 259–268.
[6] D. Guha, P.K. Roy, S. Banerjee, Load frequency control of interconnected power system using grey wolf optimization, Swarm, Evol. Comput. 27 (2016) 97–115.
[7] R.K. Sahu, S. Panda, S. Padhan, A hybrid firefly algorithm and pattern search technique for automatic generation control of multi area power systems, Int. J. Electr. Power Energy Syst. 64 (2015) 9–23.
[8] D. Guha, P.K. Roy, S. Banerjee, Quasi-oppositional differential search algorithm applied to load frequency control, Eng. Sci. Technol. 19 (4) (2016) 1635–1654.
[9] M.Y. Oozeer, R. Ramjug-Ballgobin, A jaya-based invasive weed optimization technique for load frequency control, in: Fleming P, Lacquet B, Sanei S, Deb K,

Jakobsson A. (eds.) Smart and Sustainable Engineering for Next Generation Applications. ELECOM 2018, Lecture Notes Elect Eng, vol. 561, pp. 11–21 Springer, Singapore (2019).
[10] M.T. Ozdemir, D. Ozturk, Comparative performance analysis of optimal PID parameters tuning based on the optics inspired optimization methods for automatic generation control, Energies 10 (12) (2017) 2134.
[11] E. Çelik, Improved stochastic fractal search algorithm and modified cost function for automatic generation control of interconnected electric power systems, Eng. Appl. Artif. Intell. 88 (2020) 103407.
[12] Z.Y. Yılmaz, G. Bal, E. Çelik, N. Öztürk, U. Güvenç, Y. Arya, A new objective function design for optimization of secondary controllers in load frequency control, J. Facul. Eng. Archit. Gazi Univ. 36 (4) (2021) 2053–2067.
[13] H.M. Hasanien, A. El-Fergany, Symbiotic organisms search algorithm for automatic generation control of interconnected power systems including wind farms, IET Gener. Transm. Distrib. 11 (7) (2017) 1692–1700.
[14] D. Guha, P.K. Roy, S. Banerjee, Symbiotic organism search algorithm applied to load frequency control of multi-area power system, Energy Syst. 9 (2) (2018) 439–468.
[15] N. Manoharan, S.S. Dash, K.S. Rajesh, S. Panda, Automatic generation control by hybrid invasive weed optimization and pattern search tuned 2-DOF PID controller, Int. J. Comput. Commun. Control 12 (4) (2017) 533–549.
[16] P. Satapathy, M.K. Debnath, P.K. Mohanty, Design of PD-PID controller with double derivative filter for frequency regulation, in: 2nd IEEE International Conference on Power Electronics, Intelligent Control and Energy Systems, Delhi, India, 2018, pp. 1142–1147 (2018).
[17] E. Çelik, N. Öztürk, Y. Arya, C. Ocak, (1+PD)-PID cascade controller design for performance betterment of load frequency control in diverse electric power systems, Neural Comput. Appl. (2021), https://doi.org/10.1007/s00521-021-06168-3.
[18] Z. Esfahani, M. Roohi, M. Gheisarnejad, T. Dragicevic, M.H. Khooban, Optimal non-integer sliding mode control for frequency regulation in stand-alone modern power grids, Applied Sciences 9 (2019) 1–16.
[19] A.D. Rosaline, U. Somarajan, Structured H-infinity controller for an uncertain deregulated power system, IEEE Trans. Ind. Appl. 55 (1) (2019) 892–906.
[20] L.C. Saikia, S. Mishra, N. Sinha, J. Nanda, Automatic generation control of a multi area hydrothermal system using reinforced learning neural network controller, Int. J. Electr. Power Energy Syst. 33 (4) (2011) 1101–1108.
[21] D. Sharma, S. Mishra, Non-linear disturbance observer-based improved frequency and tie-line power control of modern interconnected power systems, IET Gener. Transm. Distrib. 13 (16) (2019) 3564–3573.
[22] H.H. Ali, A.M. Kassem, M. Al-Dhaifallah, A. Fathy, Multi-Verse optimizer for model predictive load frequency control of hybrid multi-interconnected plants comprising renewable energy, IEEE Access 8 (2020) 114623–114642.
[23] M. Elsisi, M. Soliman, M.A.S. Aboelela, W. Mansour, Bat inspired algorithm based optimal design of model predictive load frequency control, Int. J. Electr. Power Energy Syst. 83 (2016) 426–433.
[24] R.K. Sahu, S. Panda, G.T. Chandra Sekhar, A novel hybrid PSO-PS optimized fuzzy PI controller for AGC in multi area interconnected power systems, Int. J. Electr. Power Energy Syst. 64 (2015) 880–893.
[25] Y. Arya, N. Kumar, Design and analysis of BFOA-optimized fuzzy PI/PID controller for AGC of multi-area traditional/restructured electrical power systems, Soft. Comput. 21 (21) (2017) 6435–6452.
[26] A.K. Barisal, T.K. Panigrahi, S. Mishra, A hybrid PSO-levy flight algorithm based fuzzy PID controller for automatic generation control of multi area power systems: fuzzy based hybrid PSO for automatic generation control, Int. J. Energy Optim. Eng. 6 (2) (2017) 42–63.
[27] M. Gheisarnejad, An effective hybrid harmony search and cuckoo optimization algorithm based fuzzy PID controller for load frequency control, Appl. Soft Comput. 65 (2018) 121–138.
[28] K.S. Rajesh, S.S. Dash, R. Rajagopal, Hybrid improved firefly-pattern search optimized fuzzy aided PID controller for automatic generation control of power systems with multi-type generations, Swarm Evol. Comput. 44 (2019) 200–211.
[29] B.K. Sahu, S. Pati, S. Panda, Hybrid differential evolution particle swarm optimization optimised fuzzy proportional-integral derivative controller for automatic generation control of interconnected power system, IET Gener. Transm. Distrib. 8 (11) (2014) 1789–1800.
[30] P.K. Mohanty, B.K. Sahu, T.K. Pati, S. Panda, S.K. Kar, Design and analysis of fuzzy PID controller with derivative filter for AGC in multi-area interconnected power system, IET Gener. Transm. Distrib. 10 (15) (2016) 3764–3776.
[31] M.K. Debnath, S. Sinha, R.K. Mallick, Application of fuzzy-PIDF controller for automatic generation control using Jaya algorithm, Int. J. Pure Appl. Math. 114 (9) (2017) 51–61.
[32] M. Gheisarnejad, M.H. Khooban, Secondary load frequency control for multi-microgrids: HiL real-time simulation, Soft. Comput. 23 (2019) 5785–5798.
[33] Y. Arya, AGC performance enrichment of multi-source hydrothermal gas power systems using new optimized FOFPID controller and redox flow batteries, Energy 127 (2017) 704–715.
[34] T. Mahto, V. Mukherjee, Fractional order fuzzy PID controller for wind energy-based hybrid power system using quasi-oppositional harmony search algorithm, IET Gener. Transm. Distrib. 11 (13) (2017) 3299–3309.
[35] A. Saha, L.C. Saikia, Utilisation of ultra-capacitor in load frequency control under restructured STPP-thermal power systems using WOA optimised PIDN-FOPD controller, IET Gener. Transm. Distrib. 11 (13) (2017) 3318–3331.
[36] E. Çelik, Design of new fractional order PI–fractional order PD cascade controller through dragonfly search algorithm for advanced load frequency control of power systems, Soft. Comput. 25 (2) (2021) 1193–1217.
[37] Y. Arya, D. Pankaj, E. Çelik, G. Sharma, H. Gözde, I. Nasiruddin, AGC performance amelioration in multi-area interconnected thermal and thermal-hydro-gas power systems using a novel controller, Eng. Sci. Technol. 24 (2) (2021) 384–396.
[38] E. Sohrabzadi, M. Gheisarnejad, Z. Esfahani, M.H. Khooban, A novel intelligent ultra-local model control-based type-II fuzzy for frequency regulation of multi-microgrids, Trans. Inst. Meas. Control 44 (5) (2022) 1134–1148.
[39] M.H. Khooban, M. Gheisarnejad, A Novel deep reinforcement learning controller based type-II fuzzy system: frequency regulation in microgrids, IEEE Trans. Emerg. Top. Comput. Intell. 5 (4) (2021) 689–699.
[40] B. Yildirim, M. Gheisarnejad, M.H. Khooban, A robust non-integer controller design for load frequency control in modern marine power grids, IEEE Trans. Emerg. Top. Comput. Intell. doi: 10.1109/TETCI.2021.3114735.
[41] M. Gheisarnejad, M.H. Khooban, J. Boudjadar, Adaptive network based fuzzy inference system for frequency regulation in modern maritime power systems, IEEE 5th International forum on Research and Technology for Society and Industry, pp. 302-307, Florence, Italy, 2019.
[42] M.H. Khooban, T. Niknam, F. Blaabjerg, T.T. Dragicevic, A new load frequency control strategy for micro-grids withconsidering electrical vehicles, Electr. Power Syst. Res. 143 (2017) 585–598.
[43] M.H. Khooban, T. Niknam, A new intelligent online fuzzy tuning approach for multi-area load frequency control: self-adaptive modified bat algorithm, Electr. Power Energy Syst. 71 (2015) 254–261.
[44] A. Oustaloup, F. Levron, B. Mathieu, F.M. Nanot, Frequency-band complex noninteger differentiator: characterization and synthesis IEEE Transactions on Circuits and Systems—I, Fund. Theory Appl. 47 (1) (2000) 25–39.
[45] B. Khokhar, S. Dahiya, K.P.S. Parmar, A novel hybrid fuzzy PD-TID controller for load frequency control of a standalone microgrid, Arab. J. Sci. Eng. 46 (2021) 1053–1065.
[46] S. Mirjalili, A.H. Gandomi, S.Z. Mirjalili, S. Saremi, H. Faris, S.M. Mirjalili, Salp swarm algorithm: a bio-inspired optimizer for engineering design problems, Adv. Eng. Softw. 114 (2017) 163–191.
[47] E. Çelik, N. Öztürk, Y. Arya, Advancement of the search process of salp swarm algorithm for global optimization problems, Expert Syst. Appl. 182 (2021) 115292.
[48] A.G. Hussien, A.E. Hassanien, E.H. Houssein, Swarming behaviour of salps algorithm for predicting chemical compound activities, in: IEEE 8th International Conference on Intelligent Computing and Information Systems, pp. 315-320, Cairo, Egypt, 2017.
[49] S. Ismael, S. Aleem, A. Abdelaziz, A. Zobaa, Practical considerations for optimal conductor reinforcement and hosting capacity enhancement in radial distribution systems, IEEE Access 6 (2018) 27268–27277.
[50] S. Ekinci, B. Hekimoglu, Parameter optimization of power system stabilizer via salp swarm algorithm, in: 5th International Conference on Electrical and Electronic Engineering, pp. 143-147, Istanbul, Turkey, 2018.
[51] S. Asaithambi, M. Rajappa, Swarm intelligence-based approach for optimal design of cmos differential amplifier and comparator circuit using a hybrid salp swarm algorithm, Rev. Sci. Instrum. 89(5) (2018) 054702.
[52] A.A. El-Fergany, Extracting optimal parameters of PEM fuel cells using salp swarm optimizer, Renewable Energy 119 (2018) 641–648.
[53] H.M. Ridha, C. Gomes, H. Hizam, S. Mirjalili, Multiple scenarios multi-objective salp swarm optimization for sizing of standalone photovoltaic system, Renewable Energy 153 (2020) 1330–1345.
[54] Y.V.K. Reddy, M.D. Reddy, Solving economic load dispatch problem with multiple fuels using teaching learning based optimization and salp swarm algorithm, J. Intell. Syst.: Theor. Appl. 1 (1) (2018) 5–15.
[55] M.T. Özdemir, D. Öztürk, İ. Eke, V. Çelik, K.Y. Lee, Tuning of optimal classical and fractional order PID parameters for automatic generation control based on the bacterial swarm optimization, IFAC-Papers On Line 48 (30) (2015) 501–506.
[56] ENTSO-E, Supporting paper for the load-frequency and reserves (Network Code European Network of Transmission System Operators for Electricity, 2013), 17–36.